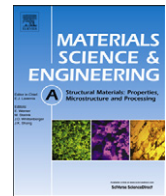




Contents lists available at [SciVerse ScienceDirect](http://www.sciencedirect.com)

Materials Science & Engineering A

journal homepage: www.elsevier.com/locate/msea



Thermo-mechanical XFEM crack propagation analysis of functionally graded materials

S.S. Hosseini, H. Bayesteh, S. Mohammadi *

School of Civil Engineering, University College of Engineering, University of Tehran, Tehran, Iran

ARTICLE INFO

Article history:

Received 26 June 2012

Received in revised form

11 October 2012

Accepted 12 October 2012

Available online 8 November 2012

Keywords:

Functionally graded material (FGM)

Extended finite element method (XFEM)

Thermal stress intensity factors

Orthotropic

Crack propagation

ABSTRACT

A computational method based on the extended finite element method (XFEM) is implemented for fracture analysis of isotropic and orthotropic functionally graded materials (FGMs) under mechanical and steady state thermal loadings. The aim is set to include the thermal effects in loading, governing equations, and the interaction integral for inhomogeneous materials with a complementary study on available crack propagation criteria in orthotropic FGMs under thermal loading conditions. The isotropic and orthotropic crack tip enrichments are applied to reproduce the singular stress field near crack tips. Mixed-mode stress intensity factors are evaluated in isotropic and orthotropic FGMs by means of the interaction integral. In addition, the mesh dependency and number of elements around the crack tip are substantially reduced in comparison with the standard finite element method with the same level of accuracy. Both mode-I and mixed-mode fracture problems with various types of mechanical and thermo-mechanical functionally graded material properties are simulated and discussed to assess the accuracy and efficiency of the proposed numerical method. Good agreements are observed between the predicted results and the reference results available in the literature with far lower degrees of freedom.

© 2012 Elsevier B.V. All rights reserved.

1. Introduction

Development of science and technology in modern world has created new challenges for engineers by employing new materials. The need for approaches to model the complex behavior of such materials is of a great importance, especially in conditions of various thermal and mechanical loadings. Materials such as steel which are suitable for mechanical loadings may lose their efficiency under thermal loadings whereas some other materials such as ceramics are more resistant against thermal loadings than mechanical effects. As a result, the idea of combination of material properties has led engineers to fabricate composites and functionally graded materials (FGM). Materials with graded variation of properties have been efficiently employed in rocket heat shields, wear resistant linings, electronically insulating metals and ceramic joints which are expected to experience high gradient temperature conditions.

FGM materials, in general have a continuously variable properties in one or more directions, preventing generation of stress singularity discontinuity. Both isotropic [1] and orthotropic [2] cases of FGMs are available and they may consist of one or more constituents [3].

Investigation of thermal effects on FGMs remains very important for two reasons. First, FGMs are affected by temperature during the manufacturing process and second, they are frequently used in structures under high thermal gradients. Hence, the study of thermal-induced stresses in FGMs is essential. Both types of steady state and transient thermal loading conditions are important [4,5].

The existence of microcracks and other defects can affect the material behavior. When the microcracks gather and propagate, form a macrocrack which can substantially affect the material behavior. Since FGMs are frequently applied under high thermal gradient conditions, it may intensify the possibility of unstable cracking.

Cracking in FGM structures has been investigated experimentally under different conditions such as impact loading [6,7], crack propagation [8,9], dynamic fracture response [10], bimaterial FGMs [11] and fracture in thermal barrier coatings (TBCs) [12]. Simultaneously, development of FGMs requires more advanced analytical and numerical methods to analyze them accurately. Hasselman and Youngblood studied the behavior of inhomogeneous material under thermo-mechanical loadings [13], and the asymptotic analysis of curved crack propagation was discussed by Abotula et al. [14]. Moreover, different types of analysis including static [14–23] and dynamic analysis [24–27] have been investigated by several researchers in recent years.

According to the thermal boundary conditions of crack surface, FGM cracks under thermal loading can be divided into insulated and non-insulated cracks. Noda and Jin considered FGM cracks in semi-infinite media as perfectly insulated [28] while Borgi and Erdogan

* Correspondence to: High Performance Computing Lab, School of Civil Engineering, University of Tehran, Tehran, Iran. Tel.: +98 21 6111 2258; fax: +98 21 6640 3808.

E-mail address: smoham@ut.ac.ir (S. Mohammadi).

studied the same cracks using partial insulation [29,30] and FGM cracks were considered partially insulated by assuming a temperature drop across the crack surfaces by Ding and Li [31]. In non-insulated cracks, the heat conduction equation is solved by neglecting the crack existence and the results are applied as a force on the structure. Several research works have been performed using different simplifications to analyze isotropic and orthotropic FGMs [32–35]. A comprehensive review on FGM thermal analysis can be found in [36].

From the numerical point of view, several studies have been devoted to crack analysis in the context of partition of unity methods, the phantom node method [37,38], meshless techniques [39–42], and the extended finite element. The extended finite element method (XFEM) is a powerful numerical tool for modeling discontinuity. XFEM is an extension of the standard finite element method which employs local enrichment of a region using the concept of partition of unity. Applying the Heaviside function in XFEM, allows for analysis of general crack propagation problems without remeshing. In addition, unlike the standard FEM which employs the ordinary polynomial-based shape functions, XFEM is capable of reproducing the complex singular stress field around a crack tip.

XFEM has been successfully used in various two [43–45] and three dimensional fracture problems [46–50], cracked plates [51] and fracture in shells [52–55]. Dolbow and Gosz studied the crack modeling in isotropic FGMs under mechanical loadings by XFEM for the first time [55]. To reproduce the exact fields at the crack tip in orthotropic media, orthotropic enrichment functions were obtained for both static [56–58] and dynamic [59,60] cases. Automatic enrichment techniques were proposed to find enrichment functions in arbitrary problems [61–64]. Furthermore, enrichment functions for interlaminar cracks in orthotropic bimetals were derived by Esna Ashari and Mohammadi [65]. XFEM has been recently employed for inhomogeneous isotropic materials under thermal loadings for static [66] and dynamic cracks by Zamani and Eslami [67]. Moreover, the natural frequencies of a cracked plate in nonhomogeneous media were obtained by XFEM using the homogenization technique [68].

Although Bayesteh and Mohammadi [69] have recently investigated fracture of orthotropic FGM materials under mechanical loadings, to the best knowledge of authors, XFEM has not been employed to crack analysis in orthotropic FGM media under thermal loadings. The main purpose of this study is to study isotropic and orthotropic FGMs under combination of mechanical and thermal loadings using XFEM. The paper begins with describing the basic formulation of FGM materials, and associated concepts of fracture mechanics, including evaluation of mixed mode stress intensity factors. Then, the XFEM model is discussed by considering the orthotropic enrichment functions, and the thermal effects on the formulation. In addition, crack propagation in orthotropic FGM materials under thermal and mechanical loadings is investigated for the first time. Finally, several numerical examples are employed to verify and compare XFEM models with the existing reference finite element models and the efficiency and accuracy of XFEM are discussed. The results may well illustrate the advantages of FGM materials compared with the homogeneous alternatives under thermal and mechanical loading conditions.

2. FGM stress–strain relationship

The total strain can be decomposed into the mechanical and thermal components,

$$\varepsilon^t = \varepsilon^m + \varepsilon^{th} \quad (1)$$

where ε^t , ε^m and ε^{th} are the total, mechanical and thermal strains, respectively. ε^m can be defined in the Lekhnitskii form of the

Hook's law [70]:

$$\varepsilon_{\alpha}^m = a_{\alpha\beta} \sigma_{\beta} \quad (\alpha, \beta = 1, 2, 6) \quad (2)$$

where

$$\varepsilon_1 = \varepsilon_{11}, \quad \varepsilon_2 = \varepsilon_{22}, \quad \varepsilon_6 = 2\varepsilon_{12} \quad (3)$$

$$\sigma_1 = \sigma_{11}, \quad \sigma_2 = \sigma_{22}, \quad \sigma_6 = \sigma_{12} \quad (4)$$

and $a_{\alpha\beta}$ can be defined from the components of material compliance tensor s_{ijkl}

$$\begin{bmatrix} a_{11} & a_{12} & a_{16} \\ a_{12} & a_{22} & a_{26} \\ a_{16} & a_{26} & a_{66} \end{bmatrix} = \begin{bmatrix} s_{1111} & s_{1122} & 2s_{1112} \\ s_{2211} & s_{2222} & 2s_{2212} \\ 2s_{1211} & 2s_{1222} & 4s_{1212} \end{bmatrix} \quad (5)$$

and

$$\varepsilon_{ij}^m = s_{ijkl} \sigma_{kl} \quad (i, j, k, l = 1, 2, 3) \quad (6)$$

In the case of plane strain, $a_{\alpha\beta}$ should be substituted by

$$\left(a_{ij} - \frac{a_{i3}a_{j3}}{a_{33}} \right) \rightarrow a_{ij} \quad (7)$$

Also, ε_{ij}^{th} can be expressed as

$$\begin{Bmatrix} \varepsilon_{11}^{th} \\ \varepsilon_{22}^{th} \\ \varepsilon_{33}^{th} \\ 2\varepsilon_{12}^{th} \end{Bmatrix} = \begin{Bmatrix} \lambda_{11} \\ \lambda_{22} \\ \lambda_{33} \\ \lambda_{12} \end{Bmatrix} \Delta T \quad (8)$$

where λ_{ij} is defined in terms of the thermal expansion coefficient α_{ij} for plane stress states

$$\lambda_{11} = \alpha_{11}, \quad \lambda_{22} = \alpha_{22}, \quad \lambda_{33} = \alpha_{33}, \quad \lambda_{12} = 0 \quad (9)$$

and for plane strain problems,

$$\lambda_{11} = \nu_{31}\alpha_{33} + \alpha_{11}, \quad \lambda_{22} = \nu_{32}\alpha_{33} + \alpha_{22}, \quad \lambda_{33} = \alpha_{33}, \quad \lambda_{12} = 0 \quad (10)$$

3. Stress intensity factors

3.1. *J*-integral

The first step in obtaining the stress intensity factors (SIFs) is to calculate the *J*-integral. Various expressions have been proposed in recent years, including the non-equilibrium, the incompatibility, and the constant-constitutive-tensor formulations, as proposed by Kim and Paulino [71]. In the present study, the incompatibility formulation is employed to approximate the *J*-integral because it requires less complicated derivatives with more or less the same level of accuracy as the non-equilibrium formulation, while the constant-constitutive-tensor method leads to unacceptable inaccuracy with the C^0 finite element formulation [71]. The incompatibility procedure is based on the following relations:

$$\sigma_{ij} = c_{ijkl}(x) \varepsilon_{kl}^m, \quad \varepsilon_{ij}^t = \frac{1}{2} (u_{i,j} + u_{j,i}), \quad \sigma_{ij,j} = 0 \quad (11)$$

which includes the constitutive and equilibrium equations and c_{ijkl} is the material modulus. The material compliance tensor s_{ijkl} can be obtained from the first relation of Eq. (11)

$$\varepsilon_{ij}^m = s_{ijkl}(x) \sigma_{kl} \quad (12)$$

In terms of the equivalent domain formulation (Fig. 1), the *J*-integral can be expressed as

$$J = \int_A (\sigma_{ij} u_{i,1} - w \delta_{1j}) q_{,j} dA + \int_A (\sigma_{ij} u_{i,1} - w \delta_{1j})_{,j} q dA \quad (13)$$

where q is a smooth function varying from $q = 1$ on the interior boundary of surface A to $q = 0$ on the outer one, as depicted in

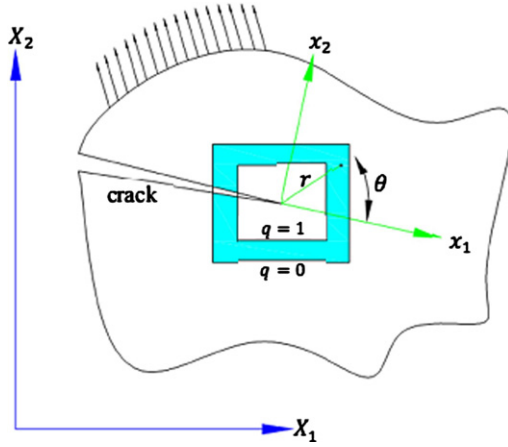


Fig. 1. Equivalent domain integral.

Fig. 1. n_j is the j th component of the outward unit normal to Γ , δ_{ij} is the Kronecker delta, the local Cartesian coordinate system x is set parallel to the crack surface and w is the strain energy density,

$$w = \frac{1}{2} (\sigma_{11} \epsilon_{11}^m + \sigma_{22} \epsilon_{22}^m + 2\sigma_{12} \epsilon_{12}^m) \quad (14)$$

which can be defined for plane stress problems as

$$w = \frac{1}{2} (\sigma_{11} \epsilon_{11}^m + \sigma_{22} \epsilon_{22}^m + \sigma_{33} \epsilon_{33}^m + 2\sigma_{12} \epsilon_{12}^m) \quad (15)$$

and for plane strain conditions,

$$\epsilon_{33}^t = 0 \rightarrow \epsilon_{33}^m = -\epsilon_{33}^t = -\alpha_{33} \Delta T \quad (16)$$

3.2. Interaction integral method

The interaction integral method is applied to calculate the mode I and II stress intensity factors. The J integral J^s for a combination of two real and auxiliary fields can be divided into three components of real J , auxiliary J^{aux} and the interaction M^l

$$J^s = J + J^{aux} + M^l \quad (17)$$

Considering

$$\sigma_{ij}^{aux} u_{i,1j} = \frac{1}{2} \sigma_{ij}^{aux} (u_{i,1j} + u_{j,1i}) = \sigma_{ij}^{aux} \epsilon_{ij,1}^t = \sigma_{ij}^{aux} (\epsilon_{ij,1}^m + \epsilon_{ij,1}^{th}) \quad (18)$$

the interaction integral M^l can be defined as

$$M^l = M^m + M^{th} \quad (19)$$

By some manipulation, M^m can be expressed as [66]

$$M^m = \int_A \left\{ \sigma_{ij} u_{i,1}^{aux} + \sigma_{ij}^{aux} u_{i,1} - \frac{1}{2} (\sigma_{ik} \epsilon_{ik}^{aux} + \sigma_{ik}^{aux} \epsilon_{ik}^m) \delta_{1j} \right\} q_j dA + \int_A \left\{ \sigma_{ij} (s_{ijkl}^{tip} - s_{ijkl}(x)) \sigma_{kl,1}^{aux} \right\} q dA \quad (20)$$

It should be mentioned that the thermal effect can be neglected in the auxiliary field and so ϵ^{aux} is reduced to the mechanical strain. Also for plane stress states,

$$\sigma_{33} \epsilon_{33}^{aux} = \sigma_{33}^{aux} \epsilon_{33}^m = 0 \quad (21)$$

and

$$\sigma_{33} \epsilon_{33}^{aux} = 0 \text{ and } \sigma_{33}^{aux} \epsilon_{33}^m \neq 0 \quad (22)$$

$$\sigma_{33} = \nu_{31} \sigma_{11} + \nu_{32} \sigma_{22} - E_{33} \alpha_{33} \Delta T \quad (23)$$

for plane stress condition.

Moreover, the thermal interaction integral is defined as

$$M^{th} = \int_A \sigma_{ij}^{aux} \epsilon_{ij,1}^{th} q dA = \int_A \sigma_{ij}^{aux} [\lambda_{ii,1} (\Delta T) + \lambda_{ii} T_{,1}] q dA \quad (24)$$

In an elastic medium, the energy release rate can be expressed as [71]:

$$G = J = c_{11} K_I^2 + c_{12} K_I K_{II} + c_{22} K_{II}^2 \quad (25)$$

with

$$c_{11} = -\frac{a_{22}}{2} \text{Im} \left(\frac{\mu_1 + \mu_2}{\mu_1 \mu_2} \right) \quad (26)$$

$$c_{12} = -\frac{a_{22}}{2} \text{Im} \left(\frac{1}{\mu_1 \mu_2} \right) + \frac{a_{11}}{2} \text{Im} (\mu_1 \mu_2) \quad (27)$$

$$c_{22} = \frac{a_{11}}{2} \text{Im} (\mu_1 + \mu_2) \quad (28)$$

where μ_i are the roots of characteristic Eq. (31). The effect of two superimposed fields can be considered as [72]

$$M^l = 2c_{11} K_I^{aux} K_I + c_{12} (K_I^{aux} K_{II} + K_{II}^{aux} K_I) + 2c_{22} K_{II}^{aux} K_{II} \quad (29)$$

Substituting $K_I^{aux} = 1$, $K_{II}^{aux} = 0$ and $K_I^{aux} = 0$, $K_{II}^{aux} = 1$ into Eq. (29), results in the following simplified simultaneous equations:

$$\begin{cases} M_1^l = 2c_{11} K_I + c_{12} K_{II} & (K_I^{aux} = 1 \text{ and } K_{II}^{aux} = 0) \\ M_2^l = c_{12} K_I + 2c_{22} K_{II} & (K_I^{aux} = 0 \text{ and } K_{II}^{aux} = 1) \end{cases} \quad (30)$$

to be solved for evaluation of actual modes I and II stress intensity factors.

3.3. Auxiliary fields

The displacement and stress fields for an orthotropic problem have already been developed by Sih et al. [73]. Since there is no explicit analytical solution for FGM problems, the homogeneous asymptotic orthotropic solution is used in the FGM condition by using the material properties at the crack tip. Applying the general methodology of the stress function $\phi = \phi(x_1 + \mu x_2)$ for the anisotropic problem, the following characteristic equation is obtained at the crack tip [70],

$$a_{11}^{tip} \mu^{tip4} - 2a_{16}^{tip} \mu^{tip3} + (2a_{12}^{tip} + a_{66}^{tip}) \mu^{tip2} - 2a_{26}^{tip} \mu^{tip} + a_{22}^{tip} = 0 \quad (31)$$

It is known that the roots μ_i^{tip} of Eq. (31) are complex and can be defined in the form of conjugate pairs, $\mu_1^{tip}, \bar{\mu}_1^{tip}$ and $\mu_2^{tip}, \bar{\mu}_2^{tip}$ [70],

$$\begin{aligned} \mu_1^{tip} &= \zeta_1 + i\beta_1 \\ \mu_2^{tip} &= \zeta_2 + i\beta_2 \end{aligned} \quad (32)$$

or sometimes in repetitive roots

$$\mu_1^{tip} = \mu_2^{tip} = \zeta + i\beta \quad (33)$$

The components of displacement in x_1 and x_2 directions can be defined as,

$$u_1^{aux} = K_I \sqrt{\frac{2r}{\pi}} \text{Re} \left\{ \frac{1}{\mu_1^{tip} - \mu_2^{tip}} \left[\mu_1^{tip} p_2^{tip} g_2^{tip}(\theta) - \mu_2^{tip} p_1^{tip} g_1^{tip}(\theta) \right] \right\} + K_{II} \sqrt{\frac{2r}{\pi}} \text{Re} \left\{ \frac{1}{\mu_1^{tip} - \mu_2^{tip}} \left[p_2^{tip} g_2^{tip}(\theta) - p_1^{tip} g_1^{tip}(\theta) \right] \right\} \quad (34)$$

$$u_2^{aux} = K_I \sqrt{\frac{2r}{\pi}} \text{Re} \left\{ \frac{1}{\mu_1^{tip} - \mu_2^{tip}} \left[\mu_1^{tip} q_2^{tip} g_2^{tip}(\theta) - \mu_2^{tip} q_1^{tip} g_1^{tip}(\theta) \right] \right\} + K_{II} \sqrt{\frac{2r}{\pi}} \text{Re} \left\{ \frac{1}{\mu_1^{tip} - \mu_2^{tip}} \left[q_2^{tip} g_2^{tip}(\theta) - q_1^{tip} g_1^{tip}(\theta) \right] \right\} \quad (35)$$

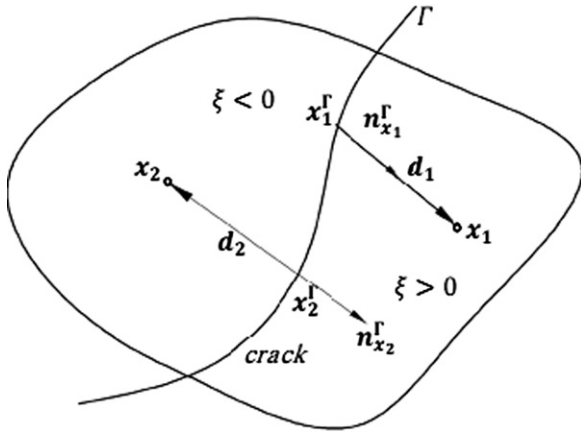


Fig. 4. Definition of the sign distance function.

traditional finite element method,

$$\mathbf{x} = \sum_{i \in \Omega} N_i(\xi, \eta) \bar{\mathbf{x}}_i \quad (49)$$

4.1. Heaviside enrichment for discontinuity

XFEM can readily simulate a discontinuity within a finite element by applying the Heaviside enrichment function,

$$H(\xi) = \begin{cases} 1 & \forall \xi > 0 \\ -1 & \forall \xi < 0 \end{cases} \quad (50)$$

where the sign distance function $\xi(\mathbf{x})$ at a point \mathbf{x} can be defined from its projection \mathbf{x}_Γ on the crack, as shown in Fig. 4.

$$\xi(\mathbf{x}) = \mathbf{d} \cdot \mathbf{n}_\Gamma^\Gamma \quad (51)$$

where

$$\mathbf{d} = \mathbf{x} - \mathbf{x}_\Gamma \quad (52)$$

and \mathbf{n}_Γ^Γ is the unit normal vector of crack line at \mathbf{x}_Γ .

The Heaviside enrichment approximation, \mathbf{u}^{He} can then be expressed as

$$\mathbf{u}^{He} = \sum_{s \in N^H} N_s(\mathbf{x}) H(\xi) \hat{\mathbf{a}}_s \quad (53)$$

4.2. Crack tip enrichments

Implementation of the crack tip enrichments leads to accurate reproduction of the highly non-linear stress and displacement fields around the crack tip. The displacement field around the crack tip can be estimated by

$$\mathbf{u}^{Tip} = \sum_{i \in N^{tip}} N_i(\mathbf{x}) \left(\sum_{k \in F} f_k(\mathbf{x}) \hat{\mathbf{b}}_{ik} \right) \quad (54)$$

where F is the set of tip enrichment functions,

$$F = \{f_1, f_2, \dots, f_m\} \quad (55)$$

N^{tip} are the enriched nodes using the tip enrichments functions and $\hat{\mathbf{b}}_{ik}$ are the extra DOFs associated with the crack tip enrichments. The crack tip enrichment functions for isotropic homogeneous materials can be defined in the form of [55]

$$F = \left\{ \sqrt{r} \sin\left(\frac{\theta}{2}\right), \sqrt{r} \cos\left(\frac{\theta}{2}\right), \sqrt{r} \sin\left(\frac{\theta}{2}\right) \sin(\theta), \sqrt{r} \cos\left(\frac{\theta}{2}\right) \sin(\theta) \right\} \quad (56)$$

Alternatively, several functions for crack tip enrichments have been proposed by Asadpour et al. [56–58], which can be expressed in a general form in the local crack-tip polar coordinate system,

$$F(r, \theta) = \left\{ \sqrt{r} \cos\left(\frac{\theta_1}{2}\right) \sqrt{g_1(\theta)}, \sqrt{r} \cos\left(\frac{\theta_2}{2}\right) \sqrt{g_2(\theta)}, \sqrt{r} \sin\left(\frac{\theta_1}{2}\right) \sqrt{g_1(\theta)}, \sqrt{r} \sin\left(\frac{\theta_2}{2}\right) \sqrt{g_2(\theta)} \right\} \quad (57)$$

with

$$g_j(\theta) = \sqrt{(\cos(\theta) + \zeta_j \sin(\theta))^2 + (\beta_j \sin(\theta))^2} \quad (j = 1, 2) \quad (58)$$

$$\theta_k(\theta) = \tan^{-1} \left(\frac{\beta_k \sin(\theta)}{\cos(\theta) + \zeta_k \sin(\theta)} \right) \quad (k = 1, 2) \quad (59)$$

where ζ_i and β_i defined in Eq. (32).

Applying the Heaviside and crack tip enrichment approximations, the displacement field can now be expressed as,

$$\mathbf{u}(\mathbf{x}) = \left[\sum_{i \in I} N_i(\mathbf{x}) \hat{\mathbf{u}}_i \right] + \left[\sum_{s \in N^H} N_s(\mathbf{x}) H(\xi(\mathbf{x})) \hat{\mathbf{a}}_s \right] + \left[\sum_{t \in N^{tip}} N_t(\mathbf{x}) \left(\sum_{k \in F} f_k(\mathbf{x}) \hat{\mathbf{b}}_{kt} \right) \right] \quad (60)$$

5. The finite element discretization

For an isotropic homogeneous system, the fully coupled thermo-mechanical set of equations can be written as,

$$k \nabla^2 T = \alpha \lambda T_0 \text{tr}(\dot{\epsilon}) + \rho c_e \dot{T} \quad (61)$$

$$\mu \nabla^2 \mathbf{u} + (\lambda + \mu) \nabla \text{tr}(\epsilon) - \alpha \lambda \nabla T = \rho \frac{\partial^2 \mathbf{u}}{\partial t^2} \quad (62)$$

where α is the volumetric coefficient of thermal expansion, k is the heat conductivity coefficient, λ and μ are the Lamé's coefficients, c_e is the specific heat at constant strain and ρ is the mass density. The thermal equation is related to the mechanical field through the $\alpha \lambda T_0 \text{tr}(\dot{\epsilon})$ term, which vanishes in static and steady state conditions: $\dot{\epsilon} = 0$. As a result, only a one-way coupling remains in (62): only the mechanical solution is affected by the thermal field.

Generalization of (61) for steady state orthotropic and non-homogeneous conditions can then be written as,

$$\frac{\partial}{\partial X_1} \left(k_{11}(X_1, X_2) \frac{\partial T(X_1, X_2)}{\partial X_1} \right) + \frac{\partial}{\partial X_2} \left(k_{22}(X_1, X_2) \frac{\partial T(X_1, X_2)}{\partial X_2} \right) = 0 \quad (63)$$

where k_{ii} is the heat conductivity coefficient along the i direction. Dirichlet and Neumann boundary conditions can be defined as

$$T = \bar{T} \quad \text{on } \Gamma_T \quad (64)$$

$$\mathbf{q}_n = \bar{\mathbf{q}} - \mathcal{G}(T - T_0) \quad \text{on } \Gamma_q \quad (65)$$

where \mathcal{G} is a transfer or radiation coefficient, T_0 is a known equilibrium value [74], $\bar{\mathbf{q}}$ is a prescribed value of $\mathbf{q} = -\mathbf{k} \nabla T$ on the boundary Γ_q and \mathbf{q}_n is the normal component of \mathbf{q} on Γ_q . \mathbf{k} is defined as:

$$\mathbf{k} = \begin{bmatrix} k_{11} & 0 \\ 0 & k_{22} \end{bmatrix} \quad (66)$$

Generally, adiabatic cracks, which contain a strong discontinuity in the temperature field, are mostly assumed in FGMs under dynamic or unsteady state (transient) conditions, whereas isothermal cracks (with a discontinuous flux) are being considered for quasi-static and steady-state solutions, usually in bimaterial FGMs. While mode I insulated (adiabatic) crack problems subjected to

certain thermal boundary conditions may well lead to a one-dimensional thermal problem, the effect of strong discontinuity, cannot be neglected in general mixed mode conditions. Nevertheless, a number of reference FGM problems [32,33] had assumed boundary conditions in such a way to avoid the direct effect of crack on thermal equation (such as a gradient parallel to the crack direction). This is certainly not the case for general thermo-mechanical crack problems, such as arbitrary inclined cracks, but as discussed by Kim and Amit [32], in steady state and static conditions for single FGM materials (and not bimetals), it is acceptable to neglect the effect of crack on the thermal results. Therefore, the solution is performed in a way where the mechanical quantities are affected by the thermal response, whereas the thermal solution is assumed to be independent of fracture and mechanical characteristics.

While approximation (60) is used to discretize the mechanical field variable u , the following isoparametric finite element approximation is implemented to discretize Eq. (63):

$$T = \sum_{i \in \Omega} N_i(\xi, \eta) \hat{T}_i \quad (67)$$

where \hat{T}_i is the temperature at node i . The final set of discretized equations can then be written as,

$$\mathbf{Q}\hat{\mathbf{T}} + \mathbf{f}^{th} = 0 \quad (68)$$

$$\mathbf{K}\mathbf{u} = \mathbf{f} \quad (69)$$

where the components of $\mathbf{Q} = Q_{ij}$, $\mathbf{f}^{th} = f_i^{th}$ and the vector $\mathbf{f} = f_i$ are defined as

$$Q_{ij} = \int_{\Omega} \mathbf{b}_i^T \mathbf{k} \mathbf{b}_j d\Omega + \int_{\Gamma_q} N_i^T \partial N_j d\Gamma \quad (70)$$

$$f_i^{th} = \int_{\Gamma_q} N_i (\bar{q} - \partial T_0) d\Gamma \quad (71)$$

where

$$\mathbf{b}_i^T = \left[\frac{\partial N_i}{\partial x_1} \quad \frac{\partial N_i}{\partial x_2} \right] \quad (72)$$

and

$$\mathbf{f} = \int_{\Omega} \mathbf{B}^T \mathbf{C} \boldsymbol{\varepsilon}^{th} d\Omega + \mathbf{f}^m \quad (73)$$

where \mathbf{B} is defined as $\boldsymbol{\varepsilon} = \mathbf{B}\hat{\mathbf{u}}$, that $\hat{\mathbf{u}}$ is all enriched and non-enriched nodal displacement vector, $\boldsymbol{\varepsilon}^{th}$ was defined in Eq. (8) and \mathbf{f}^m is part of load vector due to mechanical loading. For definitions of \mathbf{f}^m and other conventional terms, refer to [75].

6. Numerical integration

The Gauss quadrature rule is employed for numerical integration. Four and one gauss point rules are applied for the standard four-node and three-node elements, respectively. A non-cracked enriched element uses the seven-order Gauss integration. The sub-triangulation method is used to improve the accuracy of integration of cracked elements, in such a way that none of the sub-triangles include the crack, as depicted in Fig. 5 for three and four node elements. Then, 7 Gauss points are used for each sub-triangle. The total number of Gauss points depends on the number of triangles, but in average, almost 72 Gauss points are used in a tip element. Other enriched elements that do not contain any discontinuity or singularity use 7×7 Gauss points.

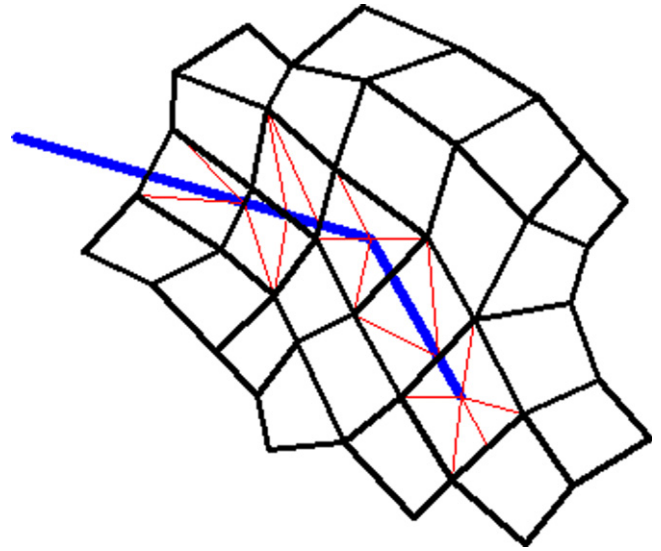


Fig. 5. Integration subtriangles around a crack.

7. Crack propagation

7.1. Isotropic criteria

Several criteria are available for crack propagation in isotropic media, including the maximum hoop stress [76], the maximum strain energy release rate [77], and the minimum strain energy density [78] criteria.

In this study, the maximum energy release rate criterion is implemented. According to Hussain et al. [75], the energy release rate for a propagation angle θ_0 can be expressed as

$$G(\theta_0) = \frac{1}{4E_{tip}} g^2(\theta_0) \left\{ (1 + 3\cos^2(\theta_0)) K_I^2 + 8\sin(\theta_0)\cos(\theta_0) K_I K_{II} + (9 - 5\cos^2(\theta_0)) K_{II}^2 \right\} \quad (74)$$

with

$$g(\theta_0) = \frac{4}{3 + \cos^2(\theta_0)} \left(\frac{1 - \theta_0/\pi}{1 + \theta_0/\pi} \right)^{\theta_0/2\pi} \quad (75)$$

where

$$E'_{tip} = \begin{cases} E_{tip} & \text{plane stress} \\ \frac{E_{tip}}{1 - \nu_{tip}} & \text{plane strain} \end{cases} \quad (76)$$

The crack propagation angle is then obtain by

$$\frac{\partial G(\theta_0)}{\partial \theta_0} = 0, \quad \frac{\partial^2 G(\theta_0)}{\partial \theta_0^2} < 0, \quad G(\theta_0) = G_{cr}(\theta_0) \quad (77)$$

where the critical energy release rate is represented by $G_{cr}(\theta_0)$:

$$G_{cr}(\theta_0) = \frac{K_{Icr}^2}{E'_{tip}} \quad (78)$$

7.2. Orthotropic criterion

In this study, two orthotropic criteria are examined. The first one is the maximum circumferential stress criterion without considering the angular change of material toughness, as proposed by Aliabadi and Sollero [79] while the second criterion is based on the maximum circumferential stress to strength

ration [80], which considers the angular change of material toughness in orthotropic materials.

The circumferential stress in terms of the Cartesian stress components can be defined as

$$\sigma_\theta = \sigma_x \sin^2 \theta + \sigma_y \cos^2 \theta - 2\sigma_{xy} \sin \theta \cos \theta \quad (79)$$

Considering Eqs. (36)–(38), this stress can be rewritten as

$$\sigma_\theta = \frac{K_I}{\sqrt{2\pi r}} \operatorname{Re}\{A(\mu_1^{\text{tip}} B_2 - \mu_2^{\text{tip}} B_1)\} + \frac{K_{II}}{\sqrt{2\pi r}} \operatorname{Re}\{A(B_2 - B_1)\} \quad (80)$$

where

$$A = \frac{1}{\mu_1^{\text{tip}} - \mu_2^{\text{tip}}}$$

$$B_i = (\mu_i^{\text{tip}} \sin(\theta) + \cos(\theta))^{1.5} \quad (81)$$

In the first approach, Eq. (80) is maximized with respect to θ in order to determine the crack extension angle. This approach does not take into account the orthotropic nature of material toughnesses, but as discussed by Aliabadi and Sollero [79], the orthotropic nature is indirectly included through the computation of stress intensity factor.

In the second approach, Saouma et al. [80] assumed that the material toughness at a typical angle θ is defined by $K_{Ic}^\omega = K_{Ic}^x \cos^2 \theta + K_{Ic}^y \sin^2 \theta$, where $(K_{Ic}^x)^{\text{tip}}$ and $(K_{Ic}^y)^{\text{tip}}$ are the toughnesses of mode I along the x_1 and x_2 directions at the crack tip, respectively. They illustrated that the angle of crack propagation (θ_0) for a general inclined crack in an anisotropic medium is

evaluated by maximizing $(K_{\theta\theta}/K_{\theta\theta c})$, which leads to, [80]

$$\frac{\sigma_\theta}{\sigma_\theta^{\max}} = \frac{K_I \operatorname{Re}\{A(\mu_1^{\text{tip}} B_1 - \mu_2^{\text{tip}} B_2)\} + K_{II} \operatorname{Re}\{A(B_1 - B_2)\}}{K_{Ic}^x \cos^2(\theta_0 + \omega) + K_{Ic}^y \sin^2(\theta_0 + \omega)} = 1 \quad (82)$$

where ω is the initial crack angle with respect to the material x_1 -axis, and θ_0 is the crack propagation angle with respect to the local crack axis, as defined in Fig. 6.

8. Numerical simulations

8.1. An FGM plate with an inclined center crack for both isotropic and orthotropic cases

A mixed-mode crack problem in the plane stress condition is considered to compare the predicted stress intensity factors for thermal and mechanical loadings with available reference results to assess the accuracy and performance of the proposed method.

The plate and crack geometry are demonstrated in Fig. 7. The crack is located at the center of the plate with length of $2a$, angle of $0 \leq \bar{\theta} \leq 90$ and $a/W = 0.1$, $L/W = 1$. The thermal loading as shown in Fig. 7(a), is applied while the top and bottom edges of plate are restrained. In Fig. 7(b), the second loading condition is assumed as the equivalent mechanical load of the thermal loading (Fig. 7(a)). For the uncracked plate, both loading conditions in the plane stress state result in a uniform strain.

For an isotropic case, the following material properties are used:

$$E^0 = 1.0, \nu = 0.3 \quad (83)$$

The nonhomogeneity parameter βa is equal to 0.5 and the variations of mechanical and thermal parameters are assumed to be exponential along the horizontal axis (X_1),

$$E(X_1) = E^0 e^{\beta X_1}, \alpha(X_1) = \alpha^0 e^{\delta X_1}, \nu(X_1) = \nu_0 \quad (84)$$

and for an orthotropic case, the reference values are

$$E_{11}^0 = 10^4, E_{22}^0 = 10^3, \nu_{12}^0 = 0.3, G_{12}^0 = 1216 \quad (85)$$

and their variations are expressed as

$$E_{11}(X_1) = E_{11}^0 e^{\beta X_1}, E_{22}(X_1) = E_{22}^0 e^{\beta X_1}, \nu_{12}(X_1) = \nu_{12}^0, G_{12}(X_1) = G_{12}^0 e^{\beta X_1} \quad (86)$$

$$\alpha_{11}(X_1) = \alpha_{11}^0 e^{\delta_1 X_1}, \alpha_{22}(X_1) = \alpha_{22}^0 e^{\delta_2 X_1} \quad (87)$$

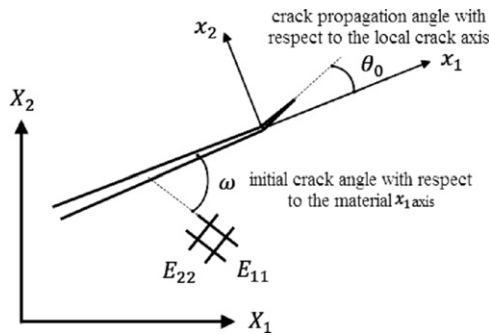


Fig. 6. Crack trajectory angle.

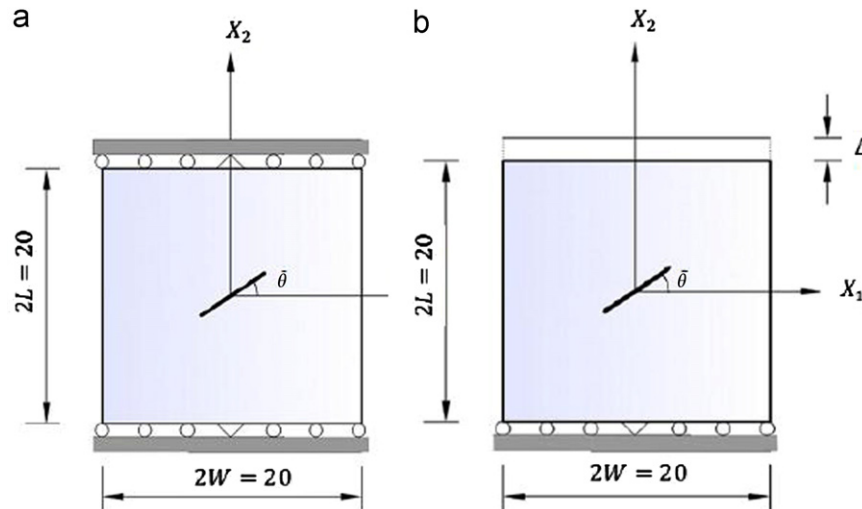


Fig. 7. Geometry of square plate under (a) thermal-induced prescribed strain, and (b) mechanical loadings.

Also, equivalent thermal and mechanical loadings are

$$(\varepsilon_{11})_{th} = (\varepsilon_{22})_{th} = -\alpha(X_1)\Delta\theta(X_1) = 1.0 \quad (88)$$

$$(\varepsilon_{22})_{mech} = \bar{\varepsilon} = \Delta/2L = 1.0 \quad (89)$$

The fixed mesh configuration for all crack angles has been shown in Fig. 8. The problem of FGM plate under thermal loading is modeled using XFEM and the results of the problem is presented for isotropic and orthotropic cases in Tables 1 and 2, respectively.

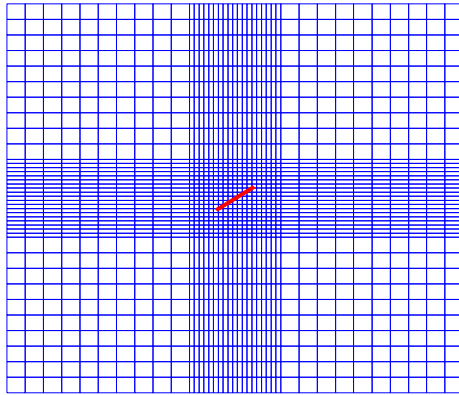


Fig. 8. Finite element mesh of the square plate.

For the isotropic case, the results are compared with the reference results for thermal loading by Kim and Paulino [32] and for equivalent mechanical loading by Konda and Erdogan [17] and Dolbow and Gosz [55]. Good agreements are observed in all cases.

For the orthotropic case, the results are obtained for both thermal and equivalent mechanical loadings using XFEM. Again, the predictions of XFEM are in good agreement with the reference results by Amit and Kim [33] under thermal and mechanical loadings for different crack angle.

Variation of normalized $|K|$ and phase angle ψ in terms of the crack angle are demonstrated for left and right tips in Fig. 9(a) and (b), respectively

$$|K| = \sqrt{K_I^2 + K_{II}^2} \quad (90)$$

$$\psi = \tan^{-1}(K_{II}/K_I) \quad (91)$$

Clearly, $|K|$ for the right tip is higher than the left one since the material properties increase along the X_1 direction. In addition, the phase angle is increased by the increase of the crack angle.

An indirect conclusion can also be made for crack propagation problems. For example, if the inclined crack was allowed to propagate, it would deviate towards the horizontal X_1 direction. This can be observed in Fig. 10 where the largest energy release rate is associated with a horizontal crack.

In order to further investigate the effect of numerical parameters on the results, the independency of normalized SIFs to

Table 1
Normalized stress intensity factors at both crack tips for the isotropic case.

$\bar{\theta}$	SIF	Left tip				Right tip			
		Thermal		Mechanical		Thermal		Mechanical	
		XFEM	[33]	[17]	[49]	XFEM	[33]	[17]	[49]
0	K_I/K_0	0.663	0.665	0.674	0.681	1.419	1.423	1.424	1.445
	K_{II}/K_0	0	0	0	0	0	0	0	0
18	K_I/K_0	0.616	0.61	0.617	0.623	1.273	1.283	1.285	1.303
	K_{II}/K_0	0.213	0.211	0.213	0.213	0.337	0.344	0.344	0.353
36	K_I/K_0	0.451	0.455	0.46	0.467	0.93	0.923	0.925	0.93
	K_{II}/K_0	0.354	0.362	0.365	0.364	0.562	0.549	0.548	0.56
54	K_I/K_0	0.249	0.245	0.247	0.251	0.48	0.488	0.49	0.488
	K_{II}/K_0	0.391	0.394	0.397	0.396	0.536	0.532	0.532	0.54
72	K_I/K_0	0.063	0.058	0.059	0.062	0.144	0.145	0.146	0.142
	K_{II}/K_0	0.245	0.266	0.269	0.268	0.344	0.314	0.314	0.316

Table 2
Normalized stress intensity factors for orthotropic case.

$\bar{\theta}$	Normalized SIF	Left tip			Right tip		
		XFEM [32]			XFEM [32]		
		Thermal	Mechanical	Thermal	Thermal	Mechanical	Thermal
0	K_I/K_0	0.659	0.66	0.666	1.429	1.426	1.428
	K_{II}/K_0	0	0	0	0	0	0
18	K_I/K_0	0.592	0.592	0.599	1.329	1.329	1.322
	K_{II}/K_0	0.227	0.227	0.244	0.246	0.246	0.216
36	K_I/K_0	0.426	0.426	0.416	1.01	1.01	1.019
	K_{II}/K_0	0.398	0.398	0.415	0.411	0.411	0.409
54	K_I/K_0	0.194	0.194	0.18	0.587	0.587	0.6
	K_{II}/K_0	0.435	0.435	0.438	0.443	0.443	0.448
72	K_I/K_0	0.027	0.027	0.006	0.216	0.216	0.216
	K_{II}/K_0	0.27	0.27	0.282	0.305	0.305	0.29

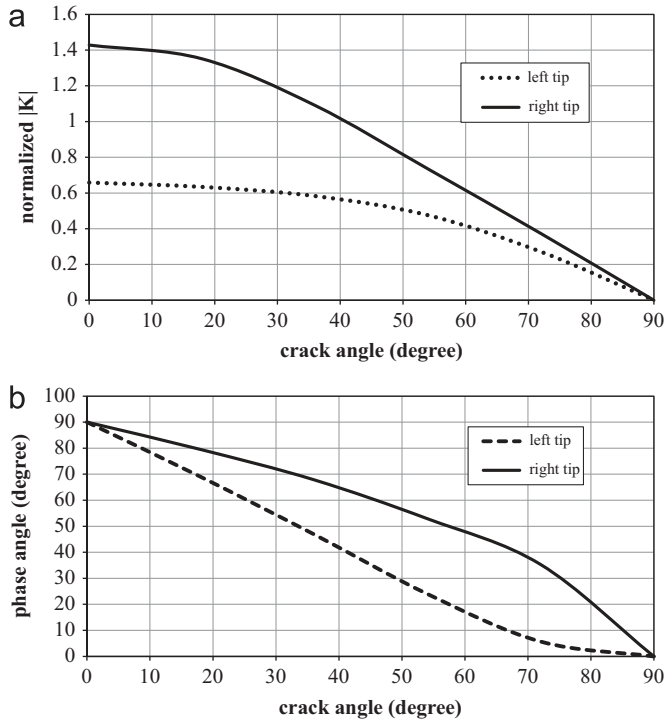


Fig. 9. (a) Variation of normalized $|K|$ versus crack angle $\bar{\theta}$ and (b) phase angle ψ versus crack angle $\bar{\theta}$ for left and right tips.

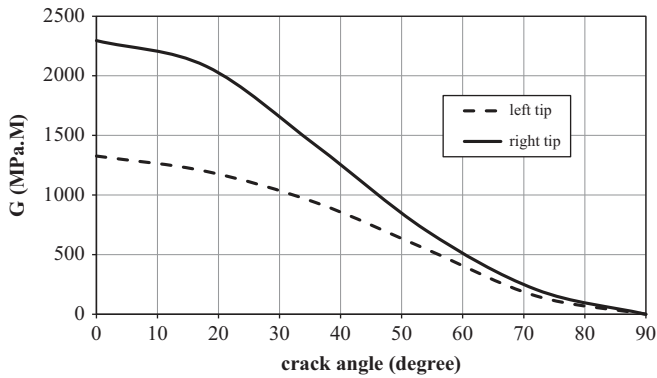


Fig. 10. Energy release rate in orthotropic condition.

radius of J -integral is examined, as depicted in Fig. 11. Clearly, the size of the J -integral domain does not notably affect the solution.

In addition, to illustrate the effect of crack tip enrichments in reproducing the exact stress field, variations of σ_{22} stress along the crack line in the crack tip element is compared with the exact homogeneous orthotropic solution in Fig. 12. While XFEM in the presence of crack tip enrichments has an excellent coincident with the exact solution, results without the crack tip enrichment dramatically deviate from the exact solution.

Comparison of the reference FGM model [32] with 5336 nodes and the present XFEM model with only 1600 nodes (less than a third) shows the higher efficiency of XFEM in comparison with the conventional numerical methods.

Several numerical simulations have shown that using large enriched area has no significant effect on the J -integral, computed from the far stress field than localized asymptotic solution. It was also observed that the optimal size of the enrichment domain may differ in various examples, but enriching a domain of radius of about $0.2a$ (where a is initial crack length) usually leads to

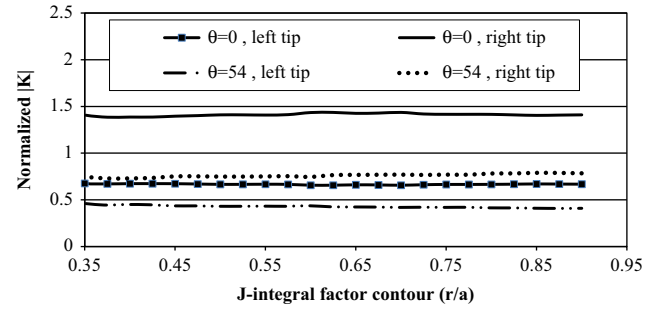


Fig. 11. Normalized $|K|$ versus radius of J -integral.

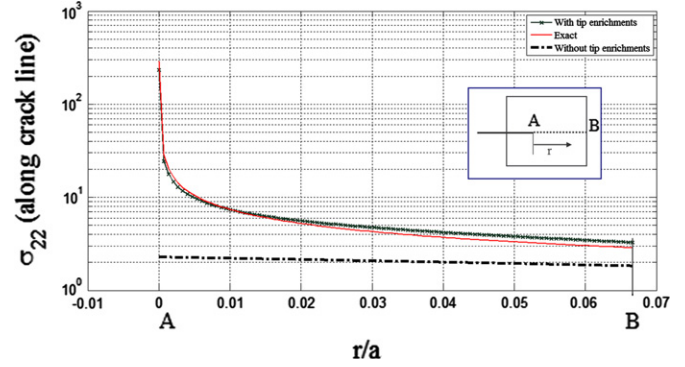


Fig. 12. Comparison of σ_{22} solution with and without crack tip enrichments (crack tip at $\theta = 0$).

quite satisfactory results. To illustrate the effect of size of the enrichment domain, Table 3 presents some of the results for the normalized stress intensity factor for various radii of enrichment domain. Clearly, the results are not sensitive to enrichment radius for both crack tips, except for $Re=0.25$ which slightly deviates from other solutions.

In addition, Fig. 13 shows the level of influence of mesh discretization on the results. It is clearly observed that by increasing the number of DOFs, the solution quickly converges and the results become mesh independent.

8.2. Edge cracked plate

An edge cracked FGM plate, depicted in Fig. 14, is considered. The upper and lower edges are constrained in the X_2 direction ($u_2 = 0$).

Variation of different parameters such as the Young's modulus, Poisson's ratio, thermal expansion coefficient and thermal conductivity coefficient can be represented in the forms of

$$E(X_1) = \frac{E^- + E^+}{2} + \frac{E^- - E^+}{2} \tan h(\beta X_1) \quad (92)$$

$$\nu(X_1) = \frac{\nu^- + \nu^+}{2} + \frac{\nu^- - \nu^+}{2} \tan h(\beta X_1) \quad (93)$$

$$\alpha(X_1) = \frac{\alpha^- + \alpha^+}{2} + \frac{\alpha^- - \alpha^+}{2} \tan h(\delta X_1) \quad (94)$$

$$k(X_1) = \frac{k^- + k^+}{2} + \frac{k^- - k^+}{2} \tan h(\delta X_1) \quad (95)$$

Both plane stress and plane strain conditions are considered with the following properties

$$a/W = 0.2-0.8, L/W = 2.0 \quad (96)$$

$$\beta = 15.0, \delta = 5.0 \quad (97)$$

Table 3
Comparison of normalized stress intensity factor for different enrichment radii.

θ	Normalized SIF	Left				Right			
		$Re=0.1$	$Re=0.15$	$Re=0.2$	$Re=0.25$	$Re=0.1$	$Re=0.15$	$Re=0.2$	$Re=0.25$
0	K_I	0.666	0.666	0.666	0.656	1.442	1.442	1.444	1.437
	K_{II}	0.000	0.000	0.000	0.000	0.000	0.000	0.000	0.000
36	K_I	0.423	0.423	0.423	0.422	1.019	1.019	1.020	1.049
	K_{II}	0.386	0.386	0.386	0.466	0.461	0.460	0.460	0.486

$$(E^-, E^+) = (1, 3), (v^-, v^+) = (0.1, 0.3), (\alpha^-, \alpha^+) = (0.01, 0.03), (k^-, k^+) = (1, 3) \quad (98)$$

The dominant size of the gradient part of the plate is governed by parameters β and δ . This is clearly observed in Fig. 15, where by increasing β , E_{22} varies more sharply in a narrower width in the central part of the plate.

The results of present XFEM are compared with the reference finite element method for the isotropic case in Table 4. The numbers of nodes in XFEM and reference models are 681 and 1001, respectively.

According to Fig. 16, a sharp change for variations of K_I occurs for $\beta=15$ when the crack tip is located within the dominant FGM part of the plate. In contrast, variations of K_I remains relatively smooth for $\beta=0$ for all cracks tip positions.

The same example is now solved for the following orthotropic material properties,

$$E = \sqrt{E_{11}E_{22}}, \quad \nu = \sqrt{\nu_{12}\nu_{21}}, \quad \delta^4 = \frac{E_{11}}{E_{22}} = \frac{\nu_{12}}{\nu_{21}}, \quad \kappa_0 = \frac{E}{2G_{12}} - \nu \quad (99)$$

$$\frac{\alpha_{11}}{\alpha_{22}} = \frac{k_{11}}{k_{22}} = \frac{E_{11}}{E_{22}} \quad (100)$$

$$E_{11}^- = 1, \quad E_{11}^+ = 3, \quad \nu_{11}^- = 0.3, \quad \nu_{11}^+ = 0.3, \quad E_{22}^+ = 3, \quad \kappa_0 = 1 \quad (101)$$

$$\alpha_{11}^- = 1, \quad \alpha_{11}^+ = 3, \quad k_{11}^- = 1, \quad k_{11}^+ = 3 \quad (102)$$

Fig. 17 shows the effect of orthotropic conditions on the mode I stress intensity factor in terms of different E_{11}/E_{22} ratios. Accordingly, by reducing E_{11}/E_{22} the first mode stress intensity factor reduces and at $E_{11}/E_{22} = 1$, the isotropic SIF is recovered.

In addition, the combined effect of orthotropy and temperature gradient on SIF is investigated in Fig. 18 for three different values of E_{11}/E_{22} . It is clearly observed that the reduction of E_{11}/E_{22} results in increase of K_I .

8.3. Thermal barrier coating with an edge crack

Surface cracks perpendicular to a coating surface occur in thermal barrier coating (TBC) problems as a result of thermal stresses. An orthotropic FGM coating on an isotropic bond coat and isotropic metal substrate is demonstrated in Fig. 19.

Periodic cracks are considered in FGM coating with the interval of $b=2$ and one of these periodic sections is modeled. The TBC is assumed at an initial temperature (T_0) and then a steady state diffusion due to different thermal boundary conditions is applied to the system.

The following specifications are employed for XFEM modeling in the plane strain condition,

$$a = 0.1-0.9, \quad b = 2 \quad (103)$$

$$W_1 = 1, \quad W_2 = 0.5, \quad W_3 = 5 \quad (104)$$

$$T_1 = T(X_1 = 0) = 0.2T_0 \text{ and } T_3 = T(X_1 = 6.5) = 0.5T_0 \quad (105)$$

with $T_0 = 1000^\circ$

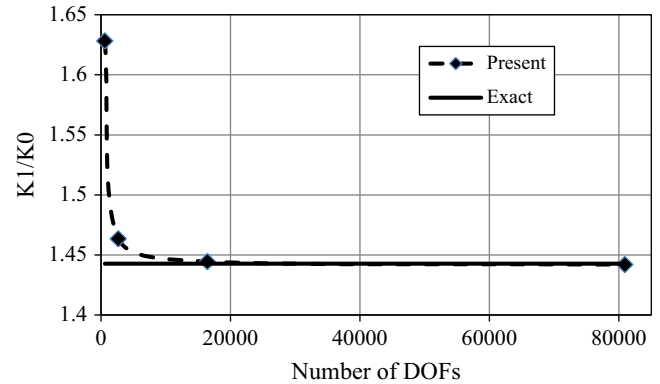


Fig. 13. Convergence of stress intensity factor for the horizontal crack problem.

Variations of material parameters for the orthotropic FGM coating region can be represented in the following forms

$$E_{11}(X_1) = E_{11}^c + (E_{bc} - E_{11}^c)X_1^2, \quad E_{22}(X_1) = E_{22}^c + (E_{bc} - E_{22}^c)X_1^2, \quad (106)$$

$$E_{33}(X_1) = E_{33}^c + (E_{bc} - E_{33}^c)X_1^2 \quad (107)$$

$$G_{12}(X_1) = G_{12}^c + (G_{bc} - G_{12}^c)X_1^2 \quad (108)$$

$$\nu_{ij}(X_1) = \nu_{ij}^c + (\nu_{bc} - \nu_{ij}^c)X_1^2 \quad (i.e., \nu_{12}, \nu_{13}, \nu_{23}) \quad (109)$$

$$\alpha_{ii}(X_1) = \alpha_{ii}^c + (\alpha_{bc} - \alpha_{ii}^c)X_1^2 \quad (i = 1, 2, 3) \quad (110)$$

$$k_{ii}(X_1) = k_{ii}^c + (k_{bc} - k_{ii}^c)X_1^2 \quad (i = 1, 2, 3) \quad (111)$$

with the reference values of

$$E_{11}^c = 27.6 \text{ GPa}, \quad E_{22}^c = 120 \text{ GPa}, \quad E_{33}^c = 50 \text{ GPa}, \quad G_{12}^c = 34 \text{ GPa} \quad (112)$$

$$\nu_{12}^c = 0.25, \quad \nu_{13}^c = 0.2, \quad \nu_{23}^c = 0.15 \quad (113)$$

$$\alpha_{11}^c = 10.01 \times 10^{-6}, \quad \alpha_{22}^c = 15 \times 10^{-6}, \quad \alpha_{33}^c = 12 \times 10^{-6} \text{ (}^\circ\text{C}^{-1}\text{)} \quad (114)$$

$$k_{11}^c = 1, \quad k_{22}^c = 5, \quad k_{33}^c = 3 \quad (115)$$

$$E_{bc} = 137.9 \text{ GPa}, \quad \nu_{bc} = 0.27, \quad \alpha_{bc} = 15.16 \times 10^{-6} \quad (116)$$

$$k_{bc} = 25 \quad (117)$$

For the isotropic FGM region:

$$E(X_1) = \frac{E_s + E_{bc}}{2} + \frac{E_s - E_{bc}}{2} \tan h(\beta X_1) \quad (118)$$

$$\nu(X_1) = \frac{\nu_s + \nu_{bc}}{2} + \frac{\nu_s - \nu_{bc}}{2} \tan h(\beta X_1) \quad (119)$$

$$k(X_1) = \frac{k_s + k_{bc}}{2} + \frac{k_s - k_{bc}}{2} \tan h(\beta X_1) \quad (120)$$

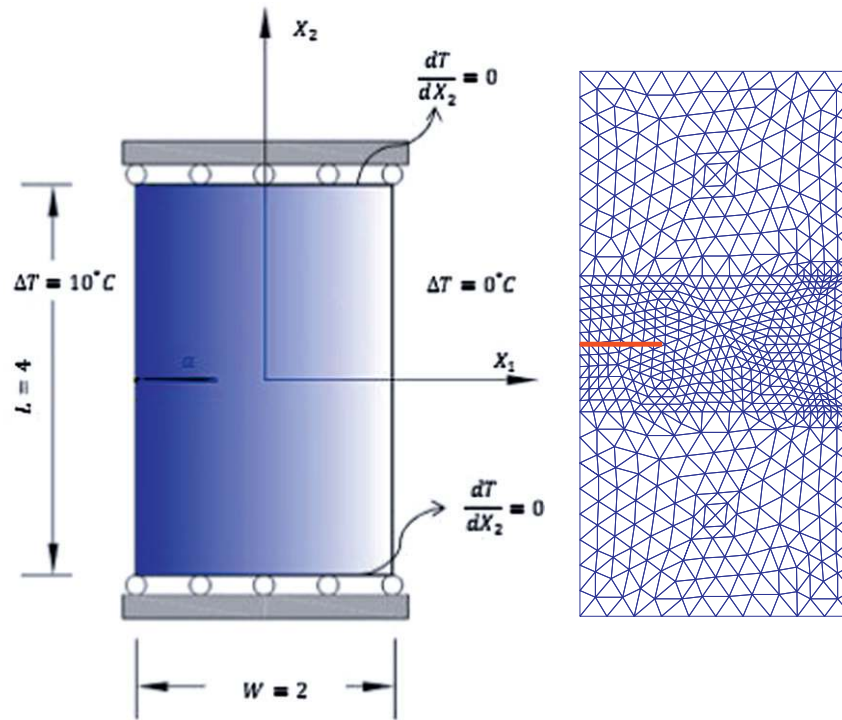


Fig. 14. Geometry and the FE mesh of the edge cracked plate.

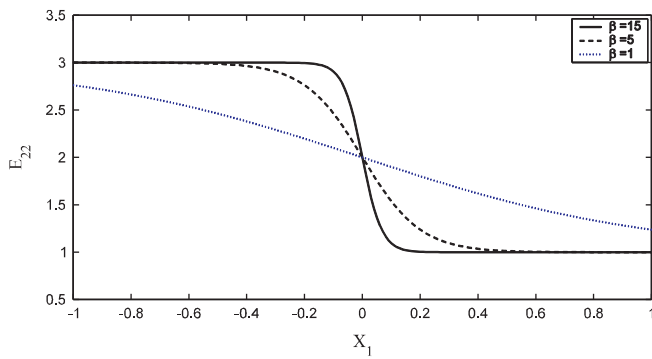
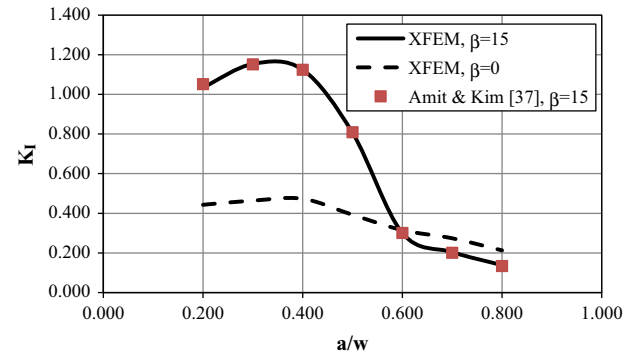
Fig. 15. Variation of E_{22} for different values of β .

Fig. 16. Variations of the first mode stress intensity factor for different positions of crack tip.

Table 4

Stress intensity factors K_I for two different β in plane stress state and isotropic condition.

a/w	$\beta = 15$		$\beta = 0$
	XFEM	FEM [33]	XFEM
0.200	1.035	1.052	0.443
0.300	1.153	1.151	0.464
0.400	1.124	1.124	0.473
0.500	0.806	0.809	0.392
0.600	0.301	0.300	0.315
0.700	0.205	0.201	0.274
0.800	0.139	0.134	0.213

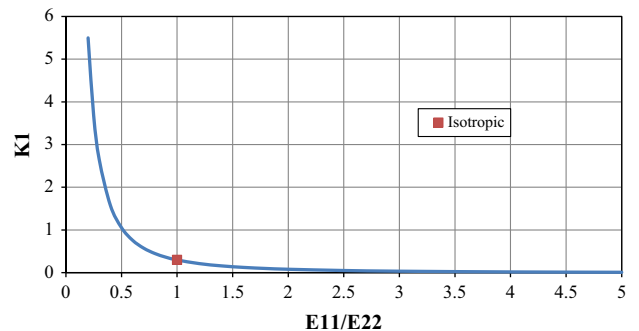


Fig. 17. The effect of orthotropy on SIF.

with

$$E_s = 175.8 \text{ GPa}, \nu_s = 0.25, \alpha_s = 13.91 \times 10^6, k_s = 7 \quad (121)$$

The solution of heat conduction Eq. (63) matches the reference results, as shown in Fig. 20. The highly non-linear variation of the

thermal field in the FGM domain is clearly distinguishable from its linear and smooth variations elsewhere.

Fig. 21 compares the XFEM predictions of stress intensity factors with the reference results. It is clearly observed that the same accuracy is obtained using 1333 nodes in XFEM model in

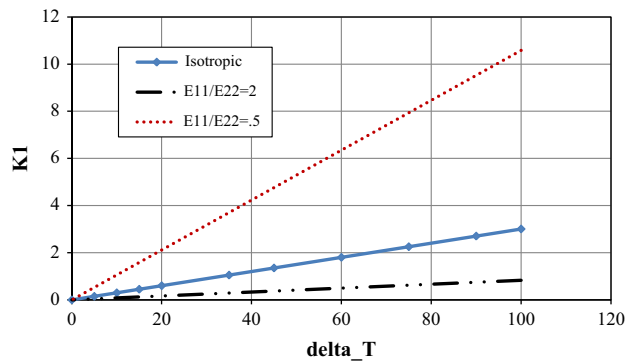


Fig. 18. Variation of SIF versus thermal gradation in different conditions.

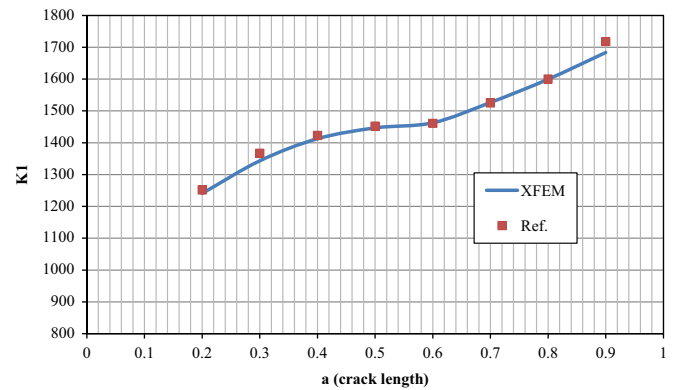


Fig. 21. SIF versus crack length.

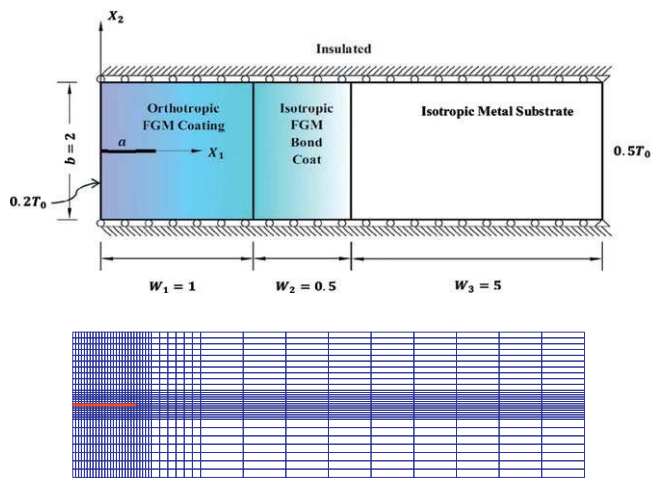


Fig. 19. Thermal barrier coating with the constituents, and the finite element mesh.

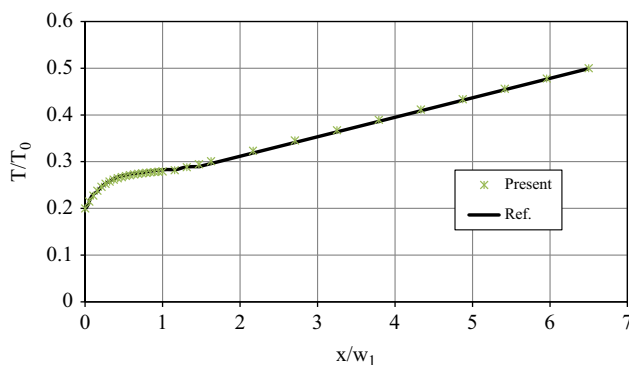


Fig. 20. The solution of heat conduction equation.

comparison with 2975 nodes used in the reference singular FEM model.

8.4. Crack propagation in FGM plate

Here, crack propagation in isotropic and orthotropic media under mechanical and thermal loadings is investigated. The geometry of the problem is demonstrated in Fig. 22 for both mechanical and thermal loadings under the plain stress condition. The following orthotropic material properties are considered:

$$\begin{aligned} E_{11}^0 &= 114.8 \text{ GPa}, E_{22}^0 = 120.84 \text{ GPa}, G_{12}^0 = 9.66 \text{ GPa}, \nu_{12}^0 \\ &= 0.21, K_{Icr}^0 = 2 \text{ Mpa}\sqrt{m} \end{aligned} \quad (122)$$

$$k_{11}^0 = 5, k_{22}^0 = 1, \alpha_{11}^0 = 15 \times 10^{-6}, \alpha_{22}^0 = 10 \times 10^{-6} \quad (123)$$

and for isotropic conditions:

$$E^0 = \sqrt{E_{11}^0 \times E_{22}^0}, \nu^0 = \sqrt{\nu_{12}^0 \times \nu_{21}^0}, G^0 = \frac{E^0}{2(1+\nu^0)} \quad (124)$$

$$k^0 = \sqrt{k_{11}^0 \times k_{22}^0}, \alpha^0 = \sqrt{\alpha_{11}^0 \times \alpha_{22}^0} \quad (125)$$

Variations of material properties are according to $P_{ij} = P_{ij}^0 \times e^{(\beta a X)}$ where $P_{ij} = E_{ij}, \nu_{ij}, G_{ij}, k_{ij}, \alpha_{ij}, K_{Icr}$ and $a = 20 \text{ mm}$ is the initial crack length. A structural quadrilateral mesh including 1325 elements and 1404 nodes is adopted, as depicted in Fig. 23.

In mechanical loading, a uniform stress is increasingly applied on the upper edge of the plate until it reaches the critical state then the crack length is increased by 2 mm increments along the calculated direction. Afterwards, the amount of uniform stress is decreased to reach the critical condition again. In the thermal problem, incremental steps are applied to T_{left} .

First, the horizontal crack problem is solved under mechanical loading for the orthotropic condition. Variation of the critical stress versus the crack length is depicted in Fig. 24 for two amounts of βa . It is observed that substantially higher stresses can be tolerated by the FGM state ($\beta a = 0.4$) compared to the homogeneous condition ($\beta a = 0$).

To consider the thermal effect on crack propagation in orthotropic FGM materials, the same problem with boundary conditions depicted in Fig. 22a is considered. The top and bottom edges are insulated and the temperature is applied on both left and right edges, for both homogeneous and inhomogeneous plates. Here, it is assumed that the right side is subjected to a constant temperature field $T_{right} = 0^\circ$ and the temperature at the left side decreases until the crack reaches the critical state. Then, the crack length is increased by $\Delta a = 2 \text{ mm}$ and the same procedure is repeated. As depicted in Fig. 25, the FGM material with $\beta a = 0.4$ can withstand more than the other one. Since both mechanical and thermal properties increase, the critical applied temperature gradient increases by the increase in total crack length. It is, however, important to note that different results are achieved if the crack is insulated or the problem is solved in an unsteady state.

In addition, mixed mode crack propagation in the isotropic condition is investigated under the thermal loading for $\beta a = 0.4$. There is a tendency for crack to further propagate in the first mode, as can be clearly seen in Fig. 26; almost negligible K_{II} in later stages of crack propagation. Furthermore, the results of critical traction for isotropic mixed mode crack propagation under mechanical loading for $\theta = 15^\circ$ and $\beta a = 0$ and 0.4 are shown in Fig. 27 where the FGM material has clearly shown higher capacity in comparison with the homogeneous one.

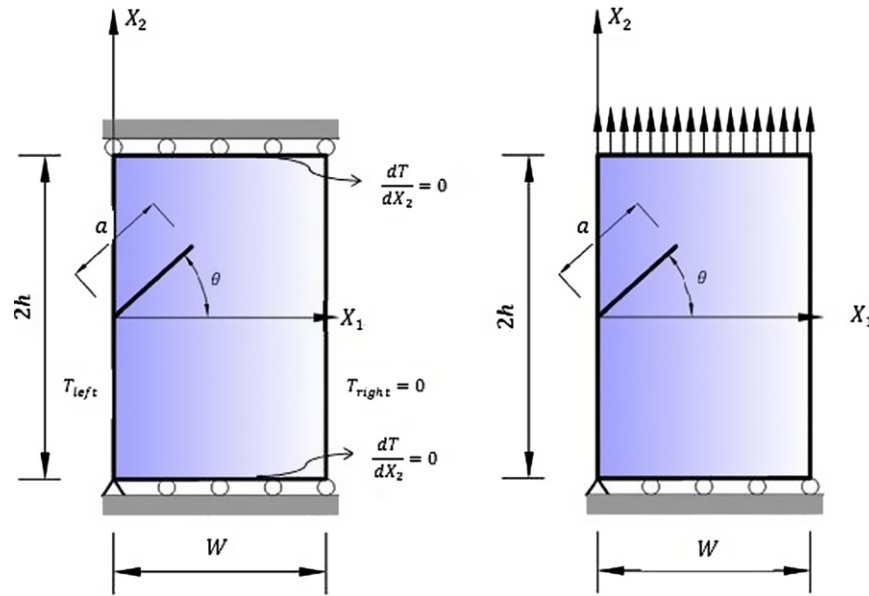


Fig. 22. The initial configuration of crack propagation in an FGM plate.

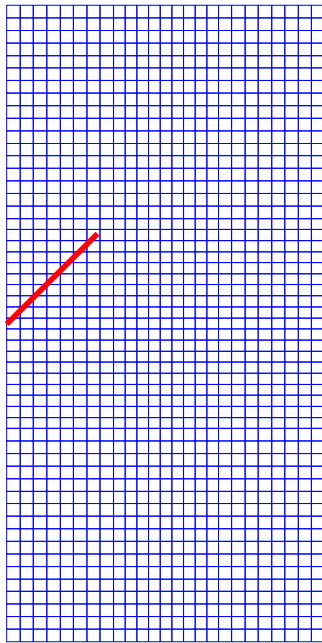


Fig. 23. The finite element mesh of the FGM plate.

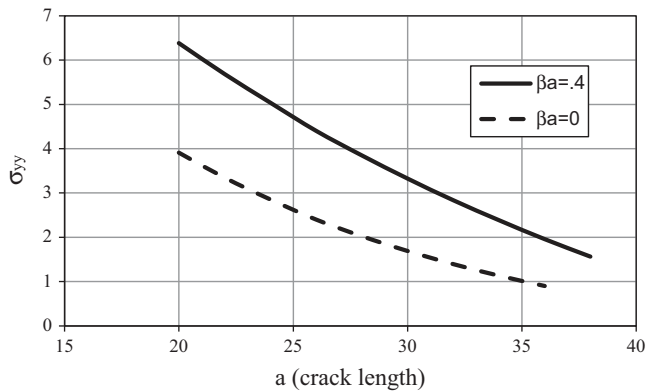


Fig. 24. Effect of non-homogeneity on maximum applied stress for different crack lengths.

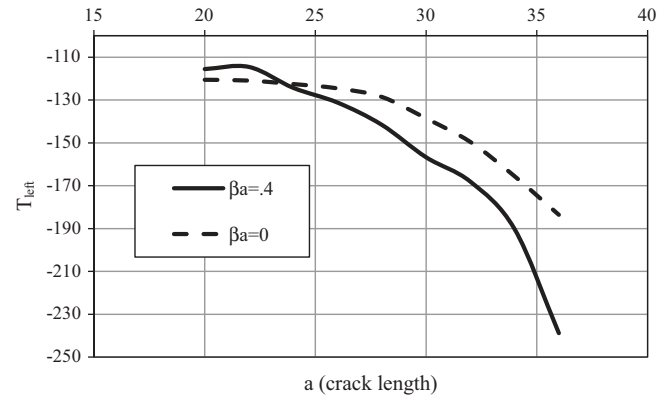


Fig. 25. Variations of the critical thermal boundary conditions on the left edge in terms of the total crack length for homogeneous and non-homogeneous orthotropic media.

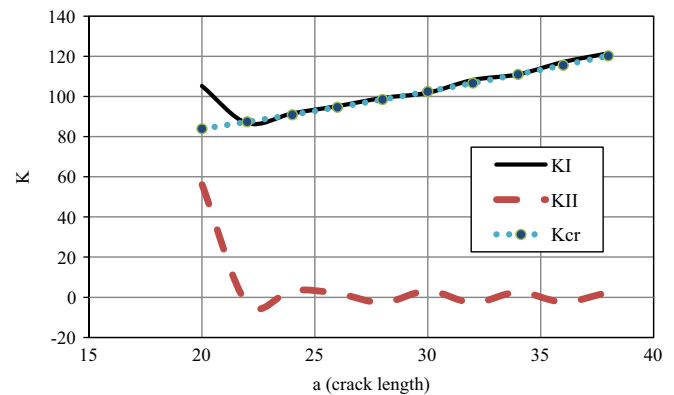


Fig. 26. Mixed mode crack propagation in isotropic media under thermal loading ($\theta = 45^\circ$, $\beta a = 0.4$).

8.5. Crack propagation in a plate with hole

To investigate the two dimensional thermal effect on mixed mode crack propagation, a square 20×20 plate with an inclined crack ($a = 2.5$ mm) emanated from the internal circular hole is

considered, as depicted in Fig. 28. The exponential FGM property variation is along the X_1 direction,

$$P_{ij} = P_{ij}^0 \times e^{(\beta a X)} \quad (\beta a = .05) \quad (126)$$

where

$$P_{ij} = E_{ij}, \nu_{ij}, G_{ij}, k_{ij}, \alpha_{ij}, K_{Icr} \quad (127)$$

A fixed finite element mesh with 2764 four-noded elements and 2868 nodes is employed for all crack propagation patterns, as depicted in Fig. 29. The thermal boundary condition is 1000 °C on all plate edges. The critical state is obtained in each step by decreasing the tolerable hole temperature. Also, a constant crack propagation length of $\Delta a = 1$ mm is used for all cases.

First, the orthotropic condition is considered,

$$E_{11}^0 = 114.8 \text{ GPa}, E_{22}^0 = 11.7 \text{ GPa}, G_{12}^0 = 9.66 \text{ GPa}, \nu_{12}^0 = 0.21, K_{Icr}^0 = 2 \text{ Mpa}\sqrt{m} \quad (128)$$

$$k_{11}^0 = 5, k_{22}^0 = 1, \alpha_{11}^0 = 15 \times 10^{-6}, \alpha_{22}^0 = 10 \times 10^{-6} \quad (129)$$

and then, an equivalent isotropic problem with two different boundary conditions are considered (see Eqs. (124) and (125))

$$E^0 = 36.649 \text{ GPa}, \nu^0 = .0214, G^0 = \frac{E^0}{2(1+\nu^0)} \quad (130)$$

$$k^0 = 2.2361, \alpha^0 = 1.2247 \times 10^{-5} \quad (131)$$

In the first isotropic case, all edges are restrained in the X_2 direction while they are free in the X_1 direction (Fig. 28a). In the second isotropic case, all the nodes on four boundary edges are restrained in both directions (Fig. 28b). The temperature

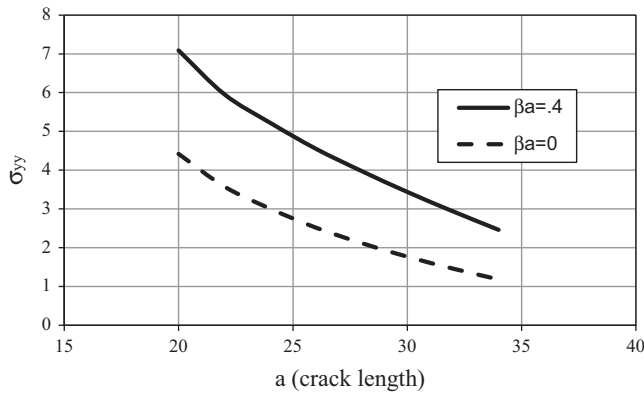


Fig. 27. Critical traction load σ_{yy} versus crack length for isotropic mixed mode crack propagation ($\theta = 15^\circ$).

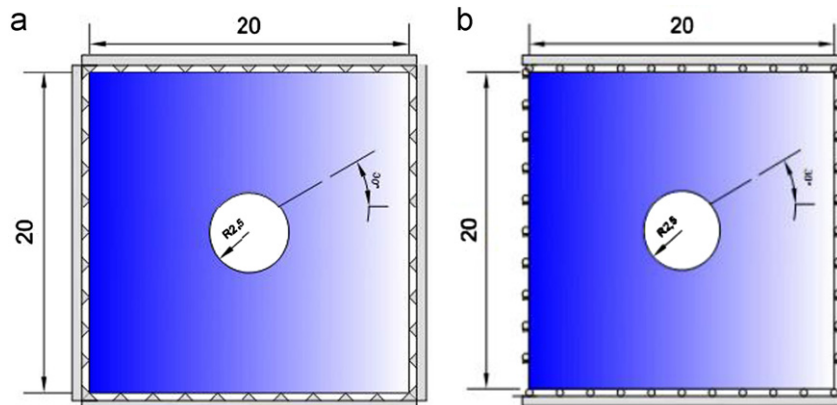


Fig. 28. Definition of geometry and boundary conditions: (a) all edges are restrained in X_1 and X_2 directions and (b) all edges are restrained in X_2 direction.

distribution contours for isotropic and orthotropic cases are depicted in Figs. 30 and 31 respectively. It is clearly observed that while a symmetric distribution is obtained in the isotropic case, the central symmetry has changed in the orthotropic case.

Variation of the critical hole temperature in terms of the crack length are depicted in Fig. 32. The existing differences for the two

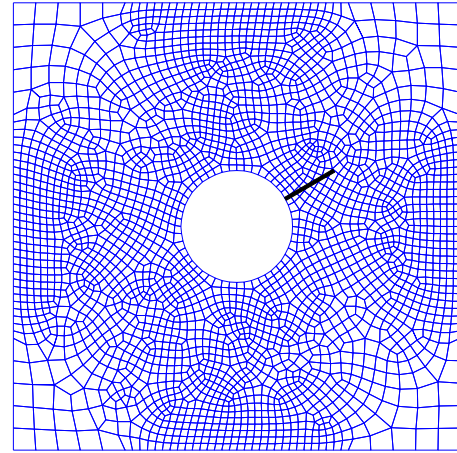


Fig. 29. The finite element mesh.

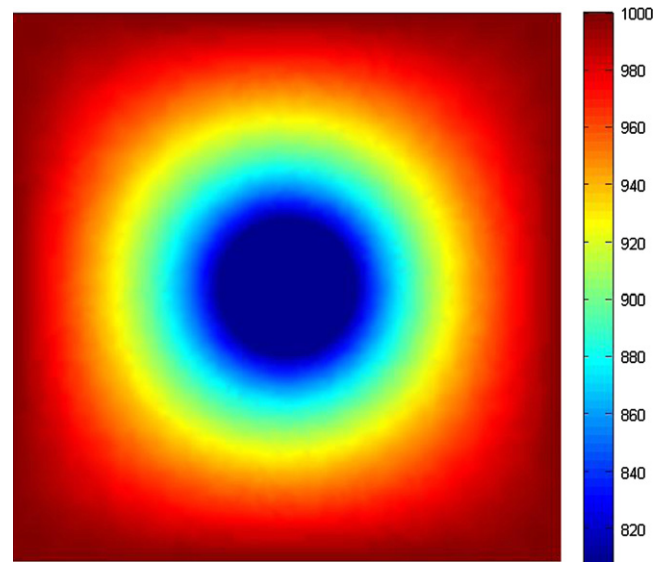


Fig. 30. Temperature distribution for the isotropic cases at first step.

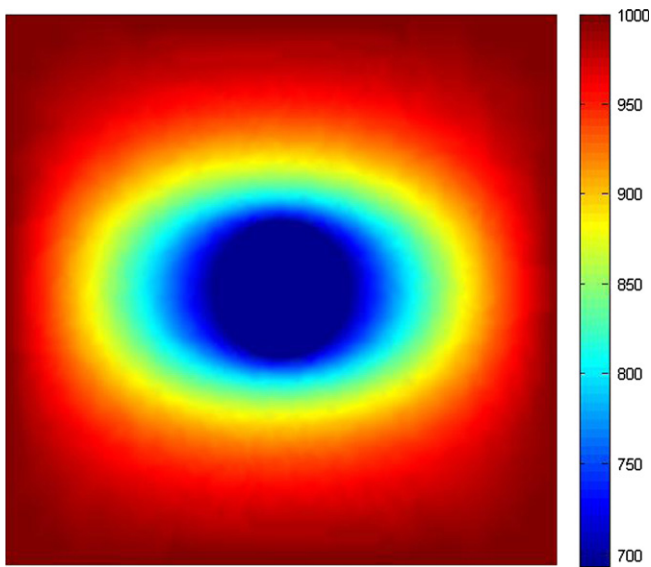


Fig. 31. Temperature distribution for the orthotropic cases at first step.

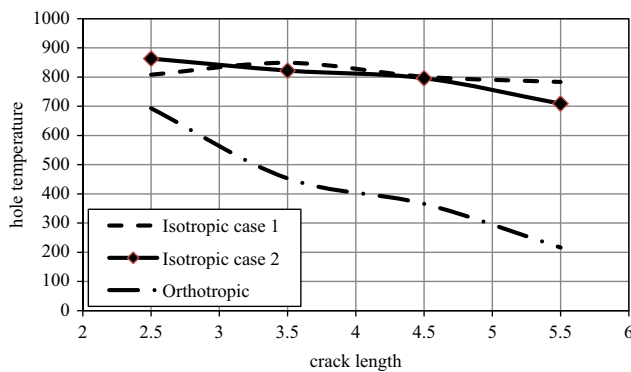


Fig. 32. Critical temperature at hole.

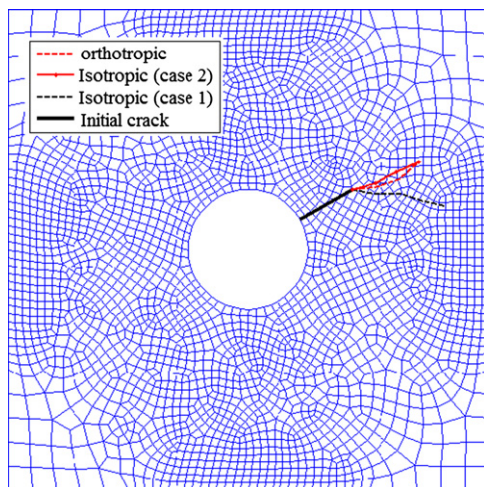


Fig. 33. Crack trajectory in isotropic and orthotropic cases.

isotropic cases can be attributed to the effects of boundary conditions. Since the tolerable hole temperature of the orthotropic case is dramatically decreased with respect to the equivalent isotropic problem, the orthotropic material can withstand substantially higher temperature gradient compared with the isotropic material properties.

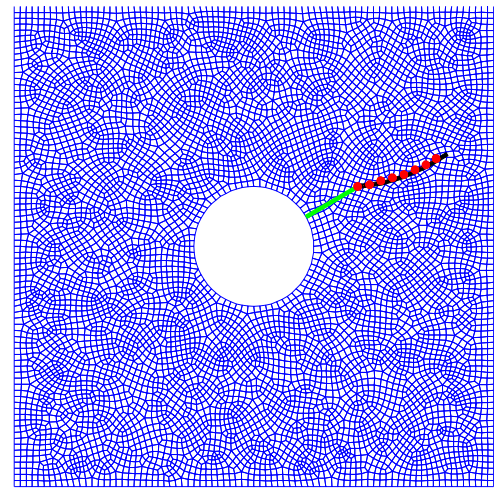


Fig. 34. Crack trajectory for different crack length increments.

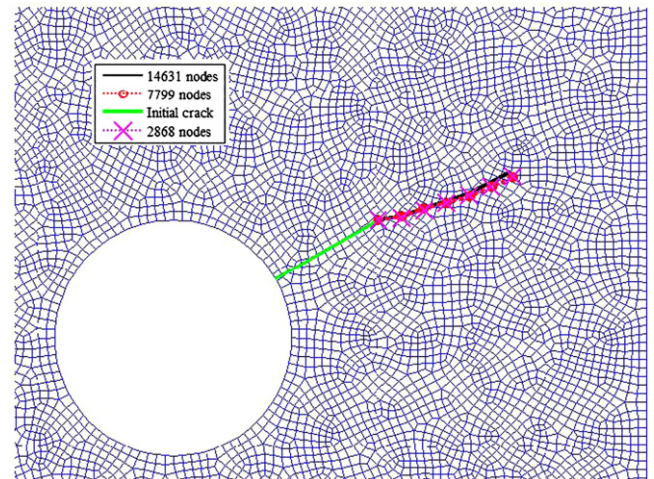


Fig. 35. Crack trajectory for different node numbers.

In addition, the predicted crack propagation trajectories for different cases are depicted in Fig. 33. In the first isotropic case, the non-symmetric boundary conditions in the two directions leads to crack rotation, while in the second one, the crack propagates almost self-similarly in the same initial direction. In the orthotropic case, the crack tends to propagate along the weakest direction.

In order to study the effect of crack length increment on predicted crack propagation trajectories, a constant hole temperature equal to 500°C for all increments is assumed. Fig. 34 depicts the crack trajectories for two different crack length increments $\Delta a = 0.5, 1$. Clearly, almost identical crack propagation paths are obtained for two different crack propagation increments. However, it should be noted that for very coarse discretizations, the results for various propagation increments may slightly differ.

In addition, the crack trajectory for different meshes under the same constant temperature conditions is depicted in Fig. 35. Again, the crack trajectories remain almost similar and coincident for different finite element meshes. Similar conclusions can be made from the displacement and stress contours at different stages of the crack propagation. Here, only sample stress contours for the initial and final steps of crack propagation are illustrated in Figs. 36 and 37.

Moreover, a comparison has been made between available crack propagation criteria to predict the propagation pattern for orthotropic FGMs. They include the orthotropic criterion based on the maximum hoop stress (ignoring the angular change of

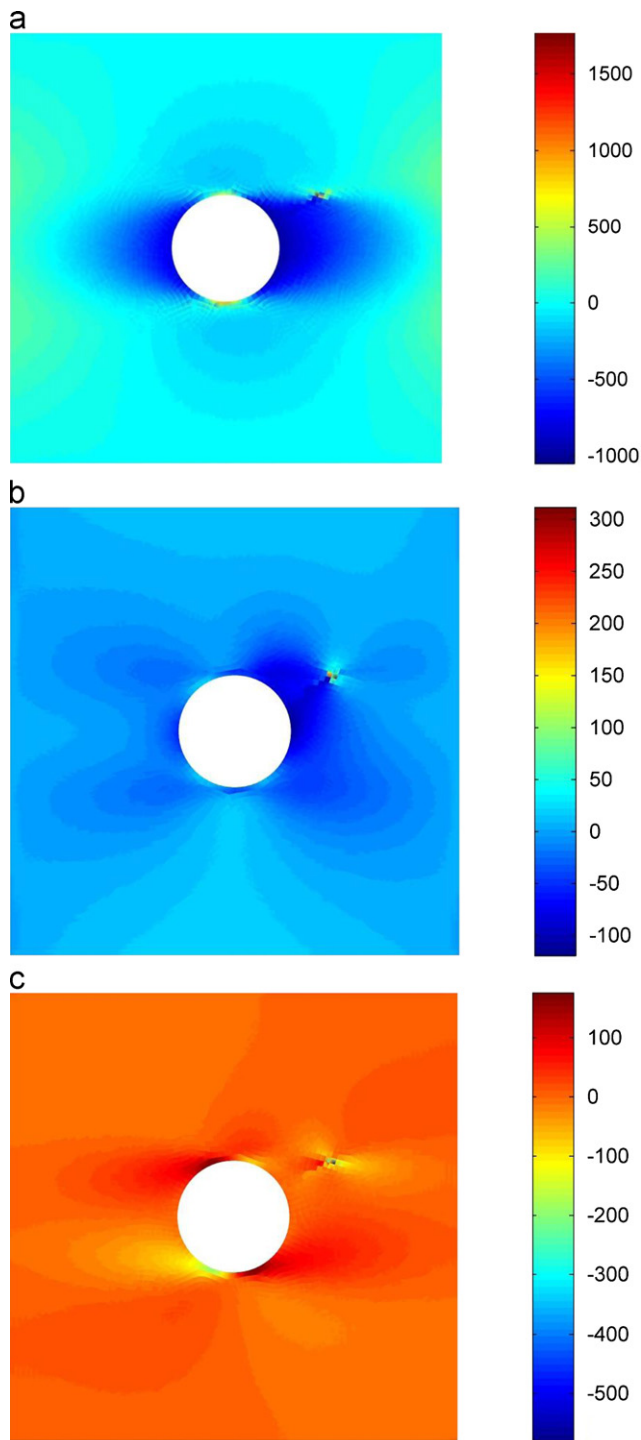


Fig. 36. Stress contours for the initial step: (a) σ_{xx} (b) σ_{yy} (c) σ_{xy} .

material toughness), and the orthotropic maximum hoop strength criterion (considering the angular change of material toughness).

Fig. 38 shows a dramatic difference between the predictions of the two approaches for the present material properties. But this not always the case. In order to further investigate the problem, another case of nearly isotropic material ($E_{11}/E_{22}=0.95$.) is considered:

$$E_{11}^0 = 114.8 \text{ GPa}, E_{22}^0 = 120.84 \text{ GPa}, G_{12}^0 = 48.67 \text{ GPa}, \nu_{12}^0 = 0.21 \quad (132)$$

Other parameters (including thermal properties) remain similar to the original model. The predicted crack propagation paths for the

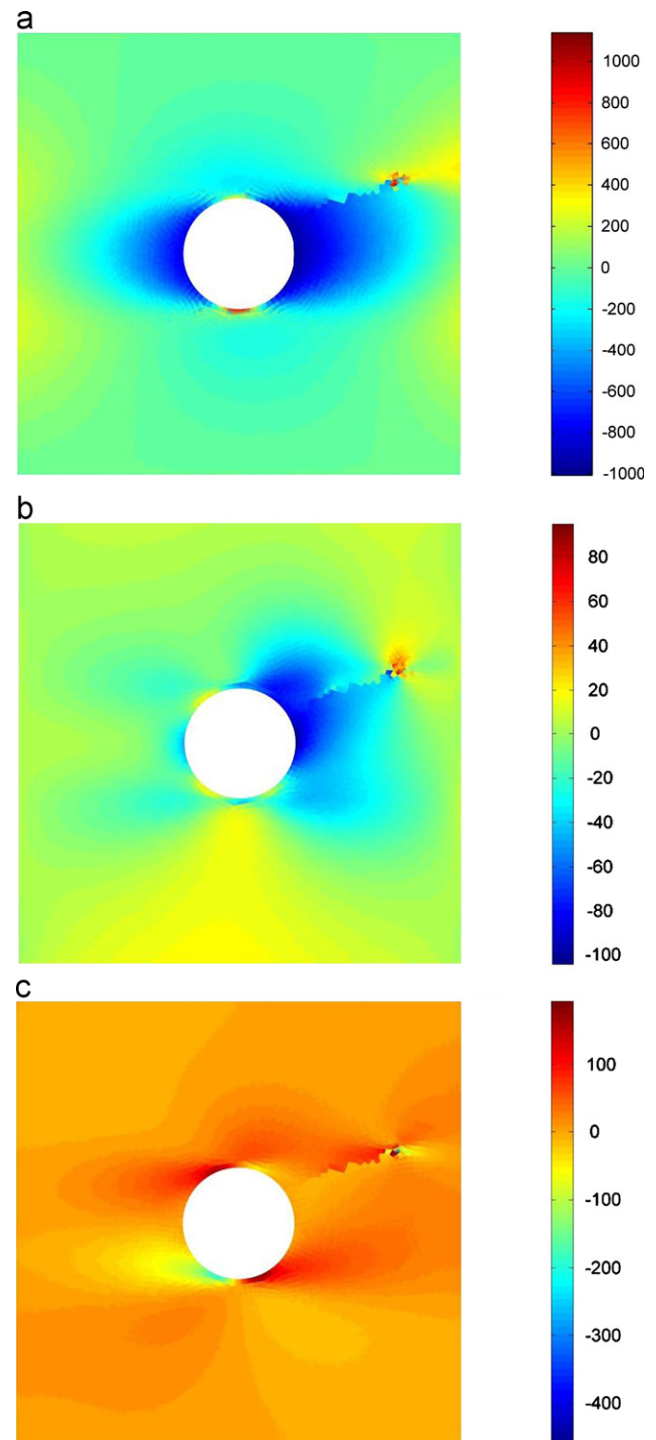


Fig. 37. Stress contours for the final step: (a) σ_{xx} (b) σ_{yy} (c) σ_{xy} .

nearly isotropic case are compared in Fig. 39. It is clearly observed that while totally two different crack trajectories are obtained from the two existing orthotropic crack propagation criteria for the case of large orthotropic ratios (Fig. 38), the crack trajectories follow a similar path as the orthotropic ratio approaches 1 (Fig. 39).

9. Conclusion

In the present study, XFEM has been employed to model FGMs under thermal and mechanical loadings. Orthotropic enrichments

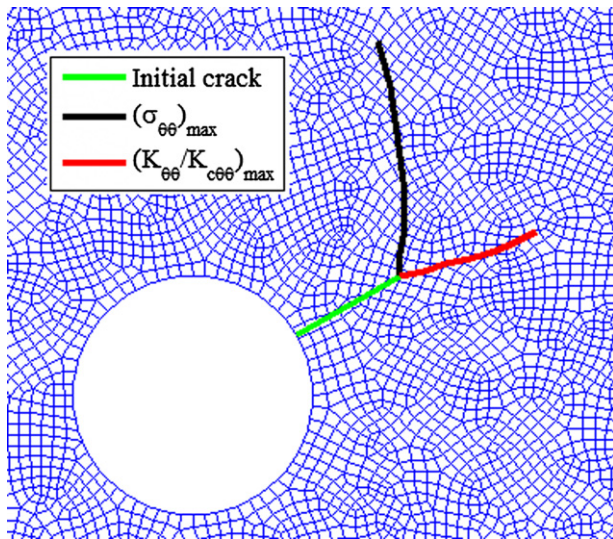


Fig. 38. Crack paths predicted by different crack propagation criteria ($E_{11}/E_{22} = 9.81$).

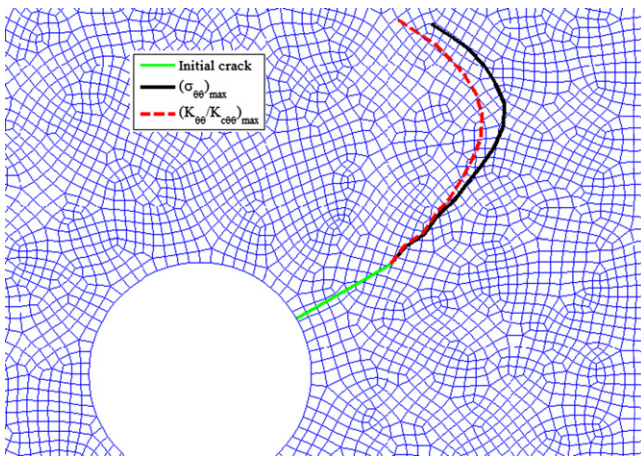


Fig. 39. Crack paths predicted by different crack propagation criteria ($E_{11}/E_{22} = 0.95$).

have been adopted for accurate solution of orthotropic media and their effects to reproduce the asymptotic crack tip stress field have been investigated. As a result, the exact singular stress field near the crack tip can be reproduced. Furthermore, implementing crack tip enrichments leads to substantial decrease of required number of DOFs compared with the standard finite element models with the same accuracy and convergence rate.

In addition, the two crack propagation formulations in orthotropic FGM media have been discussed and the effect of thermal stress on mixed mode crack propagation is investigated. The substantial differences are observed between the two criteria when the orthotropic ratio becomes larger than 1.

Moreover, comparisons have been accomplished between homogeneous and FGM materials under mechanical and thermal loadings and in all cases, FGM materials showed substantially more efficient behavior.

Acknowledgments

The authors would like to acknowledge the financial support of University of Tehran for this research under the Grant no. 8102051/1/04. Also, the technical support of the High Performance Computing

Lab, School of Civil Engineering, University of Tehran is appreciated. Furthermore, the financial support of Iran National Science Foundation (INSF) is gratefully acknowledged.

References

- [1] H.M. Yin, L.Z. Sun, G.H. Paulino, *Acta Mater.* 5 (2004) 3535–3543.
- [2] W.A. Kaysser, B. Ilshner, *MRS Bull.* 20 (1995) 22–26.
- [3] M. Nemat-Alla, *Int. J. Solids Struct.* 40 (2003) 7339–7356.
- [4] Z.-H. Jin, *Int. Commun. Heat Mass Transfer* 29 (2002) 887–895.
- [5] Y. Ootao, Y. Tanigawa, *Compos. Struct.* 63 (2004) 139–146.
- [6] H. Zhang Zhengyu, P. Glaucio, *Int. J. Plasticity* 21 (2005) 1154–1195.
- [7] A. El-Hadek Medhat, V.T. Hareesh, *Opt. Laser. Eng.* 40 (2003) 353–369.
- [8] S. Arun, J. Nitesh, *Int. J. Impact Eng.* 30 (2004) 777–803.
- [9] X.F. Yao, W. Xu, K. Arakawa, K. Takahashi, T. Mada, *Opt. Laser Eng.* 43 (2005) 195–207.
- [10] A. El-Hadek Medhat, V.T. Hareesh, *Int. J. Solids Struct.* 40 (2003) 1885–1906.
- [11] P.R. Marur, H.V. Tippur, *Int. J. Fract. Mech.* 103 (2000) 95–109.
- [12] A. Kawasaki, R. Watanabe, *Eng. Fract. Mech.* 69 (2002) 1713–1728.
- [13] D.P.H. Hasselman, G.E. Youngblood, *J. Am. Ceram. Soc.* 61 (1978) 49–52.
- [14] F. Delale, F. Erdogan, *J. Appl. Mech.* 50 (1983) 67–80.
- [15] S. Abotula, A. Kidane, V.B. Chalivendra, A. Shukla, *Int. J. Solids Struct.* (2012).
- [16] L. Schovanec, J.R. Walton, *J. Appl. Mech.* 55 (1988) 234–236.
- [17] N. Konda, F. Erdogan, *Eng. Fract. Mech.* 47 (1994) 533–545.
- [18] P. Gu, R.J. Asaro, *Int. J. Solids Struct.* 34 (1997) 1–17.
- [19] B.H. Wu, F. Erdogan, *J. Appl. Mech.* 64 (1997) 449–456.
- [20] G.H. Jin, G.H. Paulino, R.H. Dodds, *J. Appl. Mech.* 69 (2002) 370–379.
- [21] J.H. Kim, G.H. Paulino, *Int. J. Numer. Methods Eng.* 53 (2002) 1930–1935.
- [22] D.V. Kubair, P.H. Geubelle, J. Lambros, *J. Appl. Mech. Trans. ASME* 72 (2005) 461–467.
- [23] L. Zhang, J.H. Kim, *J. Appl. Mech.* 78 (2011) 1–10.
- [24] C. Atkinson, R.D. List, *Int. J. Eng. Sci.* 16 (1978) 717–730.
- [25] S. Krishnaswamy, H.V. Tippur, A.J. Rosakis, *J. Mech. Phys. Solids* 40 (1992) 339–372.
- [26] C.E. Rousseau, H.V. Tippur, *Mech. Mater.* 33 (2001) 403–421.
- [27] M.S. Kirugulige, H.V. Tippur, *Int. J. Solids Struct.* 75 (2008) 1–14.
- [28] N. Noda, Z.H. Jin, *J. Therm. Stresses* 16 (1993) 181–196.
- [29] S. El-Borgi, F. Erdogan, F.B. Hatira, *Int. J. Fract.* 123 (2003) 139–162.
- [30] S. El-Borgi, F. Erdogan, L. Hidri, *Int. J. Eng. Sci.* 42 (2004) 371–393.
- [31] S.-H. Ding, X. Li, *Arch. Appl. Mech.* 81 (2011) 943–955.
- [32] J.-H. Kim, K.C. Amit, *J. Appl. Mech.* 75 (2008).
- [33] K.C. Amit, J.-H. Kim, *Eng. Fract. Mech.* 75 (2008) 2542–2565.
- [34] S. Dag, E. Erhan Arman, B. Yildirim, *Int. J. Solids Struct.* 47 (2010) 3480–3488.
- [35] S. Dag, *Eng. Fract. Mech.* 73 (2006) 2802–2828.
- [36] V. Birman, L.W. Byrd, *Appl. Mech. Rev.* 60 (2007) 195–216.
- [37] T. Rabczuk, G. Zi, A. Gerstenberger, W.A. Wall, *Int. J. Numer. Methods Eng.* 75 (2008) 577–599.
- [38] T. Chau-Dinh, G. Zi, P.S. Lee, J.H. Song, T. Rabczuk, *Comput. Struct.* 92–93 (2012) 242–256.
- [39] T. Rabczuk, G. Zi, S. Bordas, H. Nguyen-Xuan, *Eng. Fract. Mech.* 75 (2008) 4740–4758.
- [40] T. Rabczuk, T. Belytschko, *Int. J. Numer. Methods Eng.* 61 (2004) 2316–2343.
- [41] T. Rabczuk, T. Belytschko, *Comput. Method Appl. Mech. Eng.* 196 (2007) 2777–2799.
- [42] T. Rabczuk, S. Bordas, G. Zi, *Comput. Struct.* 88 (2010) 1391–1411.
- [43] T. Belytschko, T. Black, *Int. J. Numer. Methods Eng.* 45 (1999) 601–620.
- [44] C. Daux, N. Mões, J. Dolbow, N. Sukumar, T. Belytschko, *Int. J. Numer. Methods Eng.* 48 (2000).
- [45] T. Belytschko, N. Mões, S. Usui, C. Parimi, *Int. J. Numer. Methods Eng.* 50 (2001) 993–1013.
- [46] N. Sukumar, D.L. Chopp, N. Mões, T. Belytschko, *Comput. Method Appl. Mech. Eng.* 190 (2001) 6183–6200.
- [47] N. Mões, A. Gravouil, T. Belytschko, *Int. J. Numer. Methods Eng.* 53 (2002) 2549–2568.
- [48] N. Sukumar, D.L. Chopp, B. Moran, *Eng. Fract. Mech.* 70 (2003) 29–48.
- [49] N. Sukumar, N. Mões, T. Belytschko, B. Moran, *Int. J. Numer. Methods Eng.* 48 (2000) 1549–1570.
- [50] M. Stolarska, D.L. Chopp, N. Mões, T. Belytschko, *Int. J. Numer. Methods Eng.* 51 (2001) 943–960.
- [51] J. Dolbow, N. Mões, T. Belytschko, *Int. J. Solids Struct.* 37 (2000) 7161–7183.
- [52] P.M.A. Areias, T. Belytschko, *Int. J. Numer. Methods Eng.* 62 (2005) 384–415.
- [53] E. Wyart, D. Coulon, M. Duflo, T. Pardoën, J.-F. Remacle, F. Lani, *Int. J. Numer. Methods Eng.* 72 (2007) 757–779.
- [54] H. Bayesteh, S. Mohammadi, *Comput. Mater. Sci.* 50 (2011) 2793–2813.
- [55] J. Dolbow, M. Gosz, *Int. J. Solids Struct.* 39 (2002) 2557–2574.
- [56] A. Asadpoure, S. Mohammadi, *Int. J. Numer. Methods Eng.* 69 (2007) 2150–2172.
- [57] A. Asadpoure, S. Mohammadi, A. Vafai, *Thin Wall Struct.* 44 (2006) 1031–1038.
- [58] A. Asadpoure, S. Mohammadi, A. Vafai, *Finite Elem. Anal. Des.* 42 (2006) 1165–1175.
- [59] D. Motamedi, S. Mohammadi, *Int. J. Fract. Mech.* 161 (2010) 21–39.
- [60] D. Motamedi, S. Mohammadi, *Eng. Fract. Mech.* 77 (2010) 3373–3393.

- [61] D.J. Benson, Y. Bazilevs, E. De Luycker, M.-C. Hsu, M. Scott, T.J.R. Hughes, T. Belytschko, *Int. J. Numer. Methods Eng.* 83 (2010) 765–785.
- [62] H. Waisman, T. Belytschko, *Int. J. Numer. Methods Eng.* 73 (2008) 1671–1692.
- [63] E. Chahine, P. Laborde, Y. Renard, *Math. Model. Nat. Phenom.* 4 (2009) 88–105.
- [64] A. Menk, S.P.A. Bordas, *Int. J. Numer. Methods Eng.* 83 (2010) 805–828.
- [65] S. Esna Ashari, S. Mohammadi, *Int. J. Numer. Methods Eng.* 86 (2011) 1507–1543.
- [66] L. Guo, F. Guo, H. Yu, L. Zhang, *Int. J. Solids Struct.* 49 (2012) 355–365.
- [67] A. Zamani, M.R. Eslami, *Int. J. Solids Struct.* 47 (2010) 1392–1404.
- [68] S. Natarajan, P.M. Baiz, S. Bordas, T. Rabczuk, P. Kerfriden, *Compos. Struct.* 93 (2011) 3082–3092.
- [69] H. Bayesteh, S. Mohammadi, *Compos. Pt. B Eng.* 44 (2013) 8–25.
- [70] S.G. Lekhnitskii, Holden-Day, San Francisco, 1963.
- [71] J.-H. Kim, G.H. Paulino, *J. Appl. Mech.* 72 (2005) 351–364.
- [72] S.S. Wang, J.F. Yau, H.T. Corten, *Int. J. Fract.* 16 (1980) 247–259.
- [73] G.C. Sih, P.C. Paris, G.R. Irwin, *Int. J. Fract. Mech.* (1965) 189–203.
- [74] O.C. Zienkiewicz, R.L. Taylor, J.Z. Zhu, sixth edition, Elsevier, 2005.
- [75] S. Mohammadi, Blackwell Publishing Ltd, 2008.
- [76] F. Erdogan, G.C. Sih, *J. Basic. Eng. ASME* 85 (1963) 519–527.
- [77] M. Hussain, S. Pu, J. Underwood, *ASTM Spec. Tech. Publ.* 560 (1974) 2–28.
- [78] G.C. Sih, *Int. J. Fract.* 10 (1974) 305–321.
- [79] M.H. Aliabadi, P. Sollero, *Compos. Sci. Technol.* 58 (1998) 1697–1703.
- [80] V.E. Saouma, M.L. Ayari, D.A. Leavell, *Eng. Fract. Mech.* 27 (1987) 171–189.